Characterization of LIBS emission lines for the identification of chlorides, carbonates, and sulfates in salt/basalt mixtures for the application to MSL ChemCam data

D. Anderson, B. Ehlmann, O. Forni, S. Clegg, A. Cousin, N. Thomas, J. Lasue, D. Delapp, R. Mcinroy, O. Gasnault, et al.

AGU PUBLICATIONS

JGR

Journal of Geophysical Research: Planets

RESEARCH ARTICLE
10.1002/2016JE005164

Key Points:
- Chlorine, carbon, and sulfur LIBS emission lines suited for identification and quantification of salts in a basaltic matrix were identified
- Above the measured detection limits, relative changes in salt content were observed with LIBS through univariate analysis
- Results are applicable to the investigation of salts dispersed in basaltic rock on the Martian surface with ChemCam and future instruments

Supporting Information:
- Supporting Information S1
- Data S1
- Data S2

Correspondence to:
D. E. Anderson,
deanders@caltech.edu

Citation:
Anderson, D. E., et al. (2017), Characterization of LIBS emission lines for the identification of chlorides, carbonates, and sulfates in salt/basalt mixtures for the application to MSL ChemCam data, *J. Geophys. Res. Planets*, *122*, 744–770, doi:10.1002/2016JE005164.

Received 1 SEP 2016
Accepted 13 MAR 2017
Accepted article online 20 MAR 2017
Published online 24 APR 2017

Characterization of LIBS emission lines for the identification of chlorides, carbonates, and sulfates in salt/basalt mixtures for the application to MSL ChemCam data

D. E. Anderson[1], B. L. Ehlmann[1,2], O. Forni[3], S. M. Clegg[4], A. Cousin[3], N. H. Thomas[1], J. Lasue[3], D. M. Delapp[4], R. E. McInroy[4], O. Gasnault[3], M. D. Dyar[5], S. Schröder[6], S. Maurice[3], and R. C. Wiens[4]

[1]Division of Geological and Planetary Sciences, California Institute of Technology, Pasadena, California, USA, [2]Jet Propulsion Laboratory, California Institute of Technology, Pasadena, California, USA, [3]Institut de Recherche en Astrophysique et Planétologie, Toulouse, France, [4]Los Alamos National Laboratory, Los Alamos, New Mexico, USA, [5]Department of Astronomy, Mount Holyoke College, South Hadley, Massachusetts, USA, [6]German Aerospace Center (DLR), Berlin, Germany

Abstract Ancient environmental conditions on Mars can be probed through the identification of minerals on its surface, including water-deposited salts and cements dispersed in the pore space of sedimentary rocks. Laser-induced breakdown spectroscopy (LIBS) analyses by the Martian rover Curiosity's ChemCam instrument can indicate salts, and ChemCam surveys aid in identifying and selecting sites for further, detailed in situ analyses. We performed laboratory LIBS experiments under simulated Mars conditions with a ChemCam-like instrument on a series of mixtures containing increasing concentrations of salt in a basaltic background to investigate the potential for identifying and quantifying chloride, carbonate, and sulfate salts found only in small amounts, dispersed in bulk rock with ChemCam, rather than concentrated in veins. Data indicate that the presence of emission lines from the basalt matrix limited the number of Cl, C, and S emission lines found to be useful for quantitative analysis; nevertheless, several lines with intensities sensitive to salt concentration were identified. Detection limits for the elements based on individual emission lines ranged from ~20 wt % carbonate (2 wt % C), ~5–30 wt % sulfate (1–8 wt % S), and ~5–10 wt % chloride (3–6 wt % Cl) depending on the basaltic matrix and/or salt cation. Absolute quantification of Cl, C, and S in the samples via univariate analysis depends on the cation-anion pairing in the salt but appears relatively independent of matrices tested, following normalization. These results are promising for tracking relative changes in the salt content of bulk rock on the Martian surface with ChemCam.

1. Introduction

Salts act as a tracer of past environments. As ionic solids that precipitate from aqueous fluids, salts indicate the presence of liquid water and its geochemistry, which are relevant for evaluating habitability and organics preservation potential on planetary surfaces. Assessing past and present Martian surface environments is the objective of in situ experiments performed by Curiosity, the Mars Science Laboratory rover, which is currently traversing the 155 km Gale impact crater that formed ~3.8–3.6 Ga ago on the boundary between the southern highlands and northern lowlands [*Thomson et al.*, 2011; *Le Deit et al.*, 2013]. Within the crater are alluvial fan and lacustrine deposits and a 5 km high central mound, Aeolis Mons, informally known as Mount Sharp. The sedimentary strata that constitute these features record the ancient geological and geochemical history of the region, including evidence of aqueous activity and a transition in mineralogy from clays to sulfates, potentially related to a global climate change on Mars [*Anderson and Bell*, 2010; *Milliken et al.*, 2010]. Curiosity samples the chemical composition of Gale crater rocks and sediments using a suite of instruments including ChemCam, which performs laser-induced breakdown spectroscopy (LIBS) and remote microimaging (RMI) [*Wiens et al.*, 2012; *Maurice et al.*, 2012].

LIBS is an atomic emission spectroscopy technique initiated by laser ablation of the target surface resulting in the formation of a hot (electronically excited) plasma. As the plasma cools, continuum, ionic, and atomic emissions occur, revealing the elemental composition of the sample [*Cremers and Radziemski*, 2013]. At a late stage, when the plasma has sufficiently cooled, molecular emissions can also be observed—not from molecules in the original sample but due to recombination of atoms in the plasma [e.g., *Gaft et al.*, 2014; *Forni et al.*, 2015]. ChemCam acts as a survey tool, having collected more than 422,000 spectra to date. It targets rocks

and soils at distances 1.5–7 m from the rover, analyzing spots of 350–500 μm diameter with multiple laser shots to remove dust from the surface and obtain chemical depth profiles, allowing the study of potential coatings [*Lanza et al*., 2015; *Wiens et al*., 2012; *Maurice et al*., 2012]. The wealth of data collected by ChemCam aids in directing Curiosity toward intriguing science targets for further analyses with its instrument suite [e.g., *Newsom et al*., 2016; *Frydenvang et al*., 2016; *Gasda et al*., 2016] and provides a chemical record of samples throughout the entire rover traverse.

Chlorides, carbonates, and sulfates represent classes of potential evaporite minerals that have been previously detected on the Martian surface; perchlorates and nitrates are also found in minor amounts [e.g., *Ehlmann and Edwards*, 2014; *Gendrin et al*., 2005; *Hecht et al*., 2009; *Stern et al*., 2015]. S and Cl are common bulk chemical components of Martian fine soils and rocks, as measured by the Alpha Particle X-ray Spectrometer (APXS) [e.g., *Yen et al*., 2005]. Sulfates have been detected within Mount Sharp strata from orbit [*Milliken et al*., 2010] and in situ by Curiosity in veins at multiple locations. Calcium sulfate, mostly bassanite, veins were first identified by ChemCam in Yellowknife Bay [*Nachon et al*., 2014; *Rapin et al*., 2016] and later confirmed through X-ray diffraction with Curiosity's Chemistry and Mineralogy instrument (CheMin) [*Vaniman et al*., 2014]. Sulfates were also identified in the light-toned veins of Garden City [*Nachon et al*., 2017]. In addition, LIBS molecular emission lines of CaCl have been detected from some Gale crater rocks [*Forni et al*., 2015], potentially as a result of NaCl in the rock (Ca from the accompanying host rock mixes with the Cl in the plasma to produce the CaCl molecular line that is identified in the LIBS spectrum). At Gale crater, carbonates have not yet been inferred from ChemCam data nor found at abundances $>$1–2 wt % using CheMin [*Leshin et al*., 2013]. The ChemCam spot size of 350–500 μm allows the instrument to pinpoint and measure the composition of individual salt veins. However, an outstanding question is the ability of ChemCam to detect more dispersed salts that would appear at lower concentrations in the bulk rock, for example, as detrital contributions, cementing agents, or diagenetic precipitates in the sedimentary rocks in Gale crater.

The presence of salts in bulk rocks has been inferred using ChemCam based on observed anticorrelations between the potential cation and other major elements [e.g., *Clegg et al*., 2013]; however, identification of salt anions can be a challenge. LIBS is more sensitive to elements that have low ionization energies (e.g., Na I, 5.1 eV) for which more atoms are excited in response to a particular energy input. It is less sensitive to elements with high ionization energies including chlorine (Cl I, 13.0 eV), carbon (C I, 11.3 eV), and sulfur (S I, 10.4 eV), which are crucial for identifying chloride, perchlorate, carbonate, and sulfate anions. These elements produce weak emission lines, making them more difficult to characterize than elements with prominent peaks such as alkalis, alkaline earth elements, and transition metals. The ChemCam team has therefore devoted particular attention to the measurement of Cl, C, and S in the laboratory. *Cousin et al*. [2011] developed a database of lines detectable by ChemCam under a Martian atmosphere for 32 elements focusing on controlled samples composed of a single or a small number of elements to ensure proper line identification. They identified 27 lines for Cl, 33 for C, and 28 for S. *Ollila et al*. [2011] focused on carbon, identifying 18 C peaks and 21 C_2 Swan bandheads in graphite and all 18 C peaks and 4 of the C_2 Swan bandheads in one or more geologic samples. *Lanza et al*. [2010] found that different carbonates could be distinguished from igneous materials and from each other using multivariate techniques on LIBS spectra collected under Martian conditions. Sulfur-bearing rock samples including sulfates and sulfides were used in the study by *Dyar et al*. [2011], which recommended implementing multivariate analysis of the spectral regions containing S lines around 540.08–550.10 and 559.18–567.10 nm instead of univariate analysis of the S emission lines for quantitative studies. *Schröder et al*. [2013] optimized multivariate techniques for distinguishing the spectra of eight chloride and sulfate salts and frozen salt-water solutions and selected 14 Cl and 10 S lines that were most relevant in their analysis. To complement this body of work, we conducted a systematic study of salts present at decreasing concentrations in prepared salt + basalt mixtures to address further questions regarding the influence of basaltic matrices and the detectability of salts present at low concentrations in the LIBS spectra.

Here we analyze LIBS spectra acquired for pressed pellets of salt + basalt mixtures measured in the laboratory under Martian environmental conditions with a ChemCam-like instrument so as to ultimately aid in the study of chlorine, carbon, and sulfur salt contents in Martian rock and soil targets. We build upon prior work by (1) measuring LIBS spectra of controlled mixtures of Mars-relevant salts to investigate how effects due to the basaltic matrix—typical geochemistry for Martian materials—influence the spectra and our ability to identify salt-related emission lines and (2) preparing the mixtures at several concentrations of salt relative to basalt to evaluate the potential for quantitative analysis of abundance and to establish detection thresholds. We

Table 1. Salt + Basalt Mixture Combinations[a]

Basalts		Chlorides	Carbonates	Sulfates
K1919	+	$CaCl_2$ NaCl	$CaCO_3$ *$MgCO_3$*	$CaSO_4 \cdot 2H_2O$, *$Fe_2(SO_4)_3$*, *$MgSO_4$*, *Na_2SO_4*
GBW07105	+	*NaCl*		*$CaSO_4 \cdot 2H_2O$*

[a]Each chloride, carbonate, or sulfate salt is paired with one of two basaltic backgrounds: the moderate-alkali K1919 (abbreviated here as KB) or high-alkali GBW07105 (GB). Italicized samples were measured in the second batch (see section 2).

present the spectral trends in continuum and line emission with salt concentration; identify Cl, S, and C detection thresholds; determine the best lines for use in anion detection and quantification; and then discuss how these results relate to the current literature and their applicability to the ChemCam data set and future Mars LIBS investigations.

2. Materials and Methods

2.1. Sample Preparation and Analysis

The sample set represents a selection of chlorides, carbonates, sulfates, and basalts potentially relevant to Martian surface science (Tables 1 and 2). The set is designed to investigate the effects of two variables in sample composition on the anion lines in the LIBS spectra: the cation element in the salt and the rock matrix. To this end, at least two samples of a given salt anion were included, each with a different cation. All salts were mixed with K1919, a moderate-alkali (2.27 ± 0.01 wt % Na_2O and 0.52 ± 0.01 wt % K_2O) Hawaiian basalt. In addition, for a subset of salts, a suite of salt+basalt mixtures were produced with GBW07105, a higher-alkali basalt (3.32 ± 0.01 wt % Na_2O and 2.24 ± 0.01 wt % K_2O) from the Brammer Standard Company. Salt + basalt mixtures created at various concentrations allow for quantitative analysis of anion lines through production of calibration curves (Figure 1) and the determination of Cl, C, and S detection limits in these mixtures.

Mixture preparation was as follows. Salt and basalt powder end-members were produced from reagent grade chemicals or natural rock and mineral samples (Table 2). Nonparticulate samples were crushed with a jaw crusher to produce submillimeter particles. All end-member particulates were then run through a shatterbox for several minutes to produce powders with grain sizes less than the spot size of the laser ($\leq$350 μm; see Figure S1 in the supporting information for example size distributions of the grains prior to mixing). As a result of our preparation, 85–90% of the sample is $<$250 μm. While the existence of some clumps or grains larger than the spot size is not fully ideal, we do not observe sharp discontinuities in chemistry between laser shots or surface locations, which would occur if the measurements sampled only distinct individual grains. Thus, they appear well mixed. Powders were physically mixed manually at concentrations of 5, 10, 30, 50, and 70 wt % salt with a basaltic end-member for each combination listed in Table 1. Mixtures italicized in Table 1 were also prepared at a very low salt concentration of 0.5 wt %. Elemental compositions of pure end-members and a subset of the mixtures (the 10 and 50 wt % salt mixtures of each salt + basalt series) were verified using flux-fusion inductively coupled plasma-optical emission spectroscopy for major oxides,

Table 2. End-Members and Their Sources Used in Mixtures

Sample	Origin	Source
K1919	Kilauea, Hawaii	Caltech collection, near USGS BHVO-1 locality
GBW07105	NRCCRM, China	Brammer
$MgCO_3$		Ward's
$CaCO_3$	Minas, Nuevo Leon, Mexico	Ward's
$CaSO_4 \cdot 2H_2O$	Fremont County, Colorado	Ward's
$MgSO_4$	Synthetic, reagent grade	Macron Chemicals
$Fe_2(SO_4)_3$	Synthetic, reagent grade	Carolina Chemical
Na_2SO_4	Synthetic, reagent grade	Carolina Chemical
NaCl	Synthetic, reagent grade	Macron Chemicals
$CaCl_2$	Synthetic, reagent grade	J.T. Baker
Fe_2O_3	Joan Monlevade, Minas Gerias, Brazil	Caltech Mineral Collection
SiO_2	NW end of Saline Valley, CA	Caltech Mineral Collection
$SiO_2 \cdot nH_2O$	Colton, San Bernadino Co., CA	Caltech Mineral Collection

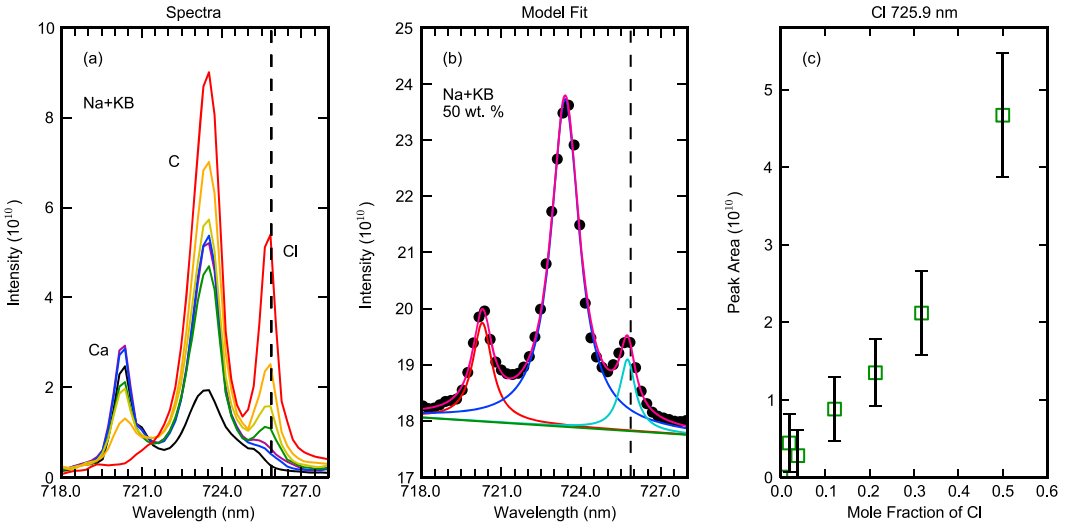

Figure 1. Example spectra, model fit, and resulting calibration curve for the Cl line at 725.9 nm in NaCl + K1919 mixtures (denoted by vertical dashed line). (a) Spectra for multiple salt concentrations are overlain after continuum removal. Colors in the spectra indicate different salt concentrations with pure basalt in black and pure salt in red, and mixtures containing salt mass fractions of 5 wt % in purple, 10 wt % in blue, 30 wt % in green, 50 wt % in yellow, and 70 wt % in orange. Intensity is in units of photons/shot/mm^2/sr/nm. (b) An example model fit to the minimally processed data (shown in black dots) of 50 wt % NaCl in K1919. The final model (shown in magenta) is the sum of three Lorentzian peaks (shown in red, blue, and cyan) with an underlying linear continuum (shown in green). (c) Peak area versus mole fraction of Cl for the mixtures based on the model fits. Peak areas are in units of photons/shot/mm^2/sr.

instrumental neutron activation analysis for Cl, and combustion in a pure oxygen environment followed by gas-phase infrared (IR) spectroscopy for C and S (measured as CO_2 and SO_2, respectively) performed by Activation Laboratories Ltd. (Actlabs) (Table S1 in the supporting information). Measured C, S, and Cl values match expected values (Figure S2).

Mixed sample powders were pressed into pellets, and LIBS analyses were performed using the ChemCam-analog instrument at Los Alamos National Laboratory [*Clegg et al*., 2017]. The instrument consists of the engineering model mast unit containing the laser, telescope, and RMI, placed inside an enclosure cooled to 14–19°C, connected by a fiber to a body unit outside the enclosure containing the optical demultiplexer, spectrometers, and data processing unit. This setup generates a maximum ChemCam laser energy of 14 mJ per pulse. Samples were analyzed with 50 consecutive laser pulses on each of five different locations on the sample surface, producing 225 spectra per sample (after excluding the first five laser shots due to potential surface effects). The experiment was performed in a chamber containing 7 torr of CO_2 to simulate a Mars-like atmosphere. Replicating the conditions under which the ChemCam data set on Mars is collected is important for making relevant comparisons to data obtained by the mission [*Cousin et al*., 2011]. Emission was collected using three detectors over the following wavelength ranges: ultraviolet (UV, 240-340 nm), blue-violet (VIO, 380-470 nm), and visible and near-infrared (VNIR, 490-850 nm). The first batch of samples was measured in September–October 2013 at a laser-to-sample distance of 1.6 m and the second batch in August–September 2014 at a distance of 3 m. The change in distance was not an ideal difference between batches but was a consequence of the setup available at the time. Distance corrections were applied during data processing to account for the viewing geometry (see sections 2.2 and 4.2). Samples from the first batch of analyses with compositions measured by Actlabs were included in the database compiled by *Clegg et al*. [2017]. The identification labels for all samples are provided in Table S2 in the supporting information. A comparison of the total integrated LIBS emission per shot for each location on a sample surface showed similar behavior among, in most cases, all five and in a few anomalous cases, at least 3–4 of the spots. This suggests that the pellet material was reasonably homogeneous.

2.2. Data Processing

Standard ChemCam data processing techniques were applied to produce clean calibrated spectra (CCS) files used for analysis of ChemCam data [*Wiens et al*., 2013]. In addition, "minimally processed" data products were

produced to preserve characteristics of the raw spectra including the continuum emission. First, the "dark" background spectrum, the median of 50 spectra collected without the laser, was subtracted from each LIBS spectrum. This removes reflected light from the sample surface, any stray light in the instrument, and instrument noise, e.g., due to dark currents. A wavelength calibration was performed by applying an offset correction derived from the comparison between a Ti reference spectrum and the median spectrum of a Ti calibration target measured on the same day as the sample. The line wavelengths are calibrated to match those obtained in a vacuum to provide appropriate comparisons to reference databases. Each spectrum was then multiplied by a smoothed gain function to correct for instrument response. Gaussian white noise was removed using the wavelet analysis method of *Wiens et al*. [2013]. The spectrum was decomposed into a series of consecutively lower resolution scales each described in terms of the wavelet basis and corresponding coefficients. A noise hard thresholding was defined at each scale by iteratively selecting wavelet coefficients less than 3× the standard deviation from the average value. After 10 iterations, wavelet coefficients less than the noise threshold were put to zero and the sum of the resulting wavelet scales became the denoised spectrum. Finally, each spectrum is corrected for geometry, including the laser-to-sample distance, and the spectral resolution of each detector element. The spectrum is divided by the approximate area of the plasma (πr^2, where $r = 0.1$ mm), solid viewing angle ($\pi(h/d)^2$, where h is half the aperture of the telescope, 54.2 mm, and d is the distance to the target), and $\Delta\lambda$, obtained by fitting a second-order polynomial to the derivative of the wavelength vector. Following the processing steps outlined above, the units of the LIBS spectral data are spectral radiance, photons/shot/mm^2/sr/nm.

Continuum emission is typically removed from the spectrum during LIBS data processing to improve visibility of the spectral lines and prior to fitting peak areas for quantitative calculations. This is justified because unlike the spectral lines, continuum emission consists of Bremsstrahlung and recombination radiation from electron-ion interactions and does not provide direct information regarding elemental abundances [*Cremers and Radziemski*, 2013]. However, theoretically determining the exact shape of the continuum emission to be removed is challenging. Therefore, in typical ChemCam LIBS processing to produce CCS files, the intensity of the continuum is determined empirically by fitting the local minima or convex hulls after a wavelet decomposition, similar to that used in denoising above [*Wiens et al*., 2013]. This continuum removal algorithm is sensitive to large peaks and overall trends of the global spectrum. Because the existing algorithm is optimized to provide a global continuum removal, it can sometimes cause the weak anion lines of interest in this study to be over or under fit, altering the shape of the spectrum and the resulting peak areas. Only a few spectral regions display an observable difference in the spectra between the CCS and minimally processed data. These include cases where two or more blended Cl lines appear at 507–510 nm (shown in Figures 2a and 2b) and 539–545 nm. However, to avoid altering our spectral regions prior to analysis, we elected to retain the continuum emission prior to peak fitting in our minimally processed spectra, and we only removed the continuum locally as part of peak area fitting for the anion lines. The sensitivity of the resulting calibration curves on this choice is discussed in section 2.4.

The spectra collected from individual laser shots were compared for different sample compositions to investigate changes in spectra due to depth into the sample or to random variation. Line intensity analyses were performed on the median spectra of shots 6–50 at the five sample locations. Median rather than mean spectra were selected to reduce the influence of outlier data. Two normalization techniques were tested: division of the area of individual channels (i.e., the intensity multiplied by $\Delta\lambda$) by the total integrated intensity of either (1) the entire spectrum resulting in a total normalized area equal to one (Norm 1) or (2) the spectral range of the detector to which the channel corresponds resulting in a total normalized area of three (Norm 3). The intensity totals were computed from the CCS files to include only the spectral lines and not the continuum. Work is ongoing to understand the applicability of normalization to atmospheric O and C lines as is typically used for H [e.g., *Rapin et al*., 2016; *Thomas et al*., 2015, 2016] for other elements. The effects of normalization on the results are described in sections 4.2 and 4.3.

2.3. Line Selection

To compare the spectral emission of different samples quantitatively, the integrated areas of emission lines of Cl, C, and S were measured. A selection of emission lines in the NIST Atomic Spectra Database [*Kramida et al*., 2015], representing elements relevant to the Martian surface with ionization levels I and II, were considered and accessed via the ChemCam Quick Element Search Tool (C-QuEST, http://pds-geosciences.wustl.edu/workshops/ChemCam_Workshop_Mar15.htm). For line identification, peak centers were allowed an uncertainty

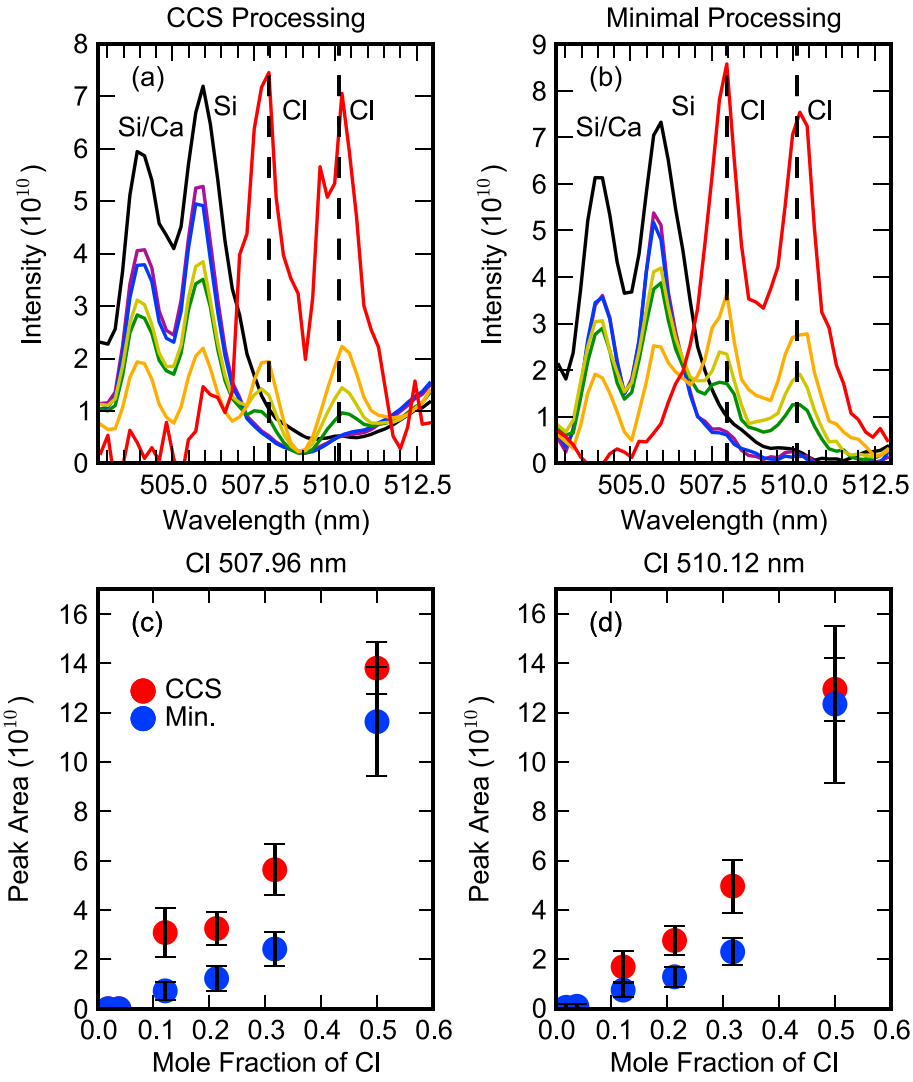

Figure 2. Comparison of (a and b) spectra and (c and d) calibration curves between CCS (Figure 2a, red dots in Figures 2c and 2d) and minimally processed data (Figure 2b, blue dots in Figures 2c and 2d) for peaks at 507.9 and 510.1 nm in NaCl + K1919 mixtures. This example displays the uncommon case in which the resultant spectra are different, following the different data processing steps. Colors in the spectra indicate different salt concentrations with pure basalt in black, pure salt in red, and mixtures containing salt mass fractions of 5 wt % in purple, 10 wt % in blue, 30 wt % in green, 50 wt % in yellow, and 70 wt % in orange. Intensity is in units of photons/shot/mm^2/sr/nm. Despite differences in the spectra, similar increasing trends are observed in the calibration curves. Peak areas are in units of photons/shot/mm^2/sr.

from the reference wavelength within ±1.0× the ChemCam spectrometer resolution (~0.2 nm for wavelengths <470 nm and ~0.65 nm for wavelengths >470 nm). All emission lines in the C-QuEST database for the element of interest (C, S, or Cl) were searched for in the LIBS data from a mixture suite by using an algorithm that checked for increasing line intensity with concentration as indicated by a positive slope between the intensity at the reference wavelength and the mole fraction of the element ($\chi_{element}$). Lines were ranked based on the value of this slope, with high values indicating a greater sensitivity and the R^2 indicating a linear correlation. Line emission is expected to increase with the number of emitting atoms (mole fraction) in a linear fashion when excluding complicating effects such as self-absorption at high abundances of the element or presence of the element in the blank (in our case, the pure basalt). Linear trends would provide the best ability to distinguish signals across a large range of concentrations improving quantification. However, emission lines were not excluded based on lack of linear trends since any monotonically increasing trend could be useful for some level of quantification. The increasing trends in the height of potential peaks with salt concentration in this subset of high-ranking lines were then visually verified by examination of the spectra.

Comparing a given spectral region among all salt + basalt mixtures, pure end-members, and additional mixture sets including SiO_2 + K1919, $SiO_2 \cdot nH_2O$ + K1919, and Fe_2O_3 + K1919 aided in identification of elemental lines. To avoid confusion with lines of other elements, the initial criteria for identification of anion lines that may be useful for univariate analysis in the mixture spectra were the following: (1) a visually detectable peak appeared above the level of the background emission at the location of the reference wavelength; (2) the peak was sufficiently free from interference such that it could be visually distinguished and fit separately from neighboring peaks; (3) the line strength generally increased with salt concentration, giving the calibration curve a positive slope; and (4) the line identity was supported by spectral comparison between mixtures, including those not containing the element in question. Stricter criteria to further select lines useful for future quantitative analyses based on our results were (5) a detection threshold of ~50 wt % salt or less regardless of mixture composition, (6) the line strength increased monotonically with salt concentration for high salt concentrations (with preference toward monotonically increasing trends starting at lower concentrations and with steeper slopes), and (7) reliable behavior independent of the chemistry of the matrix and host phase of the element of interest.

2.4. Fitting of Spectral Peaks

For lines identified according to the criteria outlined in section 2.3, the local spectral region was fit, using a Levenberg-Marquardt algorithm [*Gill et al*., 1981] as part of the LMFIT Python package [*Newville et al*., 2014] to model a spectrum composed of Lorentzian functions for all observable peaks and an underlying linear continuum. The local region to be fit was selected to include any nearby peaks of the same element, any peaks that interfered with or contributed to the peak of interest, and a local region where the continuum could be reasonably approximated by including a linear function (Figures 1a and 1b). Simplified peak and continuum shapes were chosen to limit the use of excess free parameters. The number of peaks included in the model and their locations were determined based on those visibly present in the spectrum combined with knowledge provided in the C-QuEST data. Free parameters optimized with the Levenberg-Marquardt algorithm were the continuum slope and its intercept as well as central wavelength, width, and height for each Lorentzian peak. Thus, each spectral region was fit with 3N+2 parameters, where *N* is the number of peaks. There were a minimum of 1.5 to a maximum of 9.4 spectral data points per parameter. Peak areas were computed with corresponding error estimates using the formula described by *Fabre et al*. [2014]: [(uncertainty in width/width) + (uncertainty in intensity/intensity)] × area. Uncertainties of one standard deviation on individual parameters were taken from the estimated covariance matrix.

Calibration curves were generated by plotting peak area versus mole fraction of element (χ). An example curve and the corresponding spectra are shown in Figure 1. We plot against mole fraction because fundamentally the strength of LIBS emission lines depends on the number of atoms producing emission rather than the mass of these atoms (or wt %). The mole fraction is calculated from the theoretical chemical formula of the salt and the elemental composition of the basalt based on the ActLabs analysis (Table S1). This excludes the hydration state of the salt. Future work will focus on characterizing the hydration of these mixtures using the H peak [e.g., *Thomas et al*., 2015, 2016; *Sobron et al*., 2012; *Rapin et al*., 2016]. Peak area was selected rather than peak height because the total intensity of a single atomic emission line is typically spread over multiple spectral channels, and this method can better account for contributions to the line strength from interfering neighboring lines [*Singh and Thakur*, 2007]. A local continuum versus global continuum fit affects the parameterization of the fit (curve shape and slope) but not the overall judgment as to the utility of the line (Figures 2c and 2d).

2.5. Calculation of Limits of Detection

For the analysis of unknown samples on the Martian surface, it is important to understand the lower limit of detectable salt concentrations. Three methods were used to determine the detection limits of Cl, C, and S in these mixtures following the example of *Wiens et al*. [2013] and *Lasue et al*. [2012]. The first method (limit of detection 1, LOD1) defines the lowest measured concentration in the sample set where the line emission appears significantly above the noise. This threshold was determined by identifying the lowest salt concentration for which the height of emission at the elemental line location is greater than 3× the standard deviation of the noise in the data prior to denoising. Peaks were only considered if they were centered on the same wavelength as the corresponding peak in the pure salt therefore excluding peaks due to matrix elements present near the line location at lower salt concentrations. The second method (LOD2) defines the

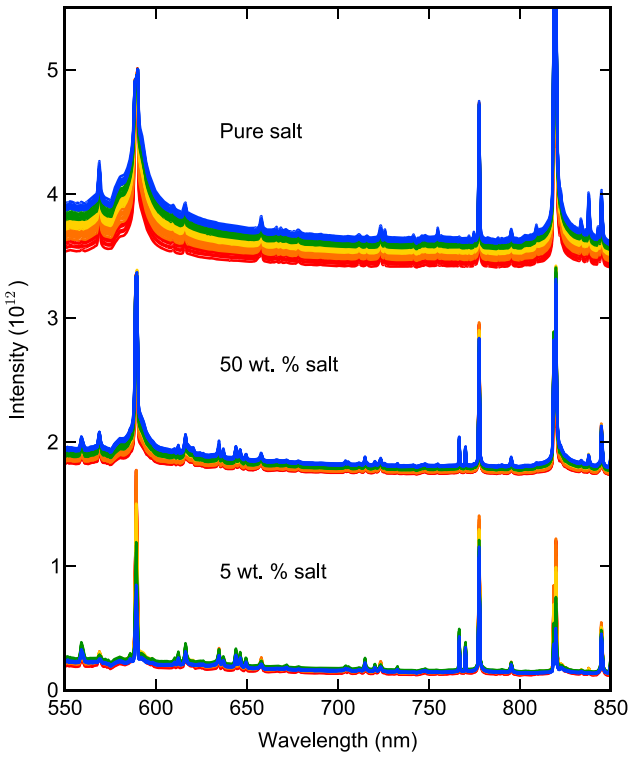

Figure 3. Processed LIBS spectra show an increase in intensity of continuum emission with shot number for NaCl + K1919 mixtures with increasing salt concentration over the wavelength range from 550 to 850 nm, a representative sample of the full spectrum. Colors correspond to shot numbers: red is shots 1–10, orange is 11–20, yellow is 21–30, green is 31–40, and blue is 41–50. Intensity is in units of photons/shot/mm^2/sr/nm. Absolute intensity for each salt concentration is offset by 1.6×10^{12} for the 50 wt % salt and 3.2×10^{12} for the pure salt to aid in visual comparison.

concentration at which the signal is significantly above the blank [*Cremers and Radziemski*, 2013], in this case the spectrum of the basaltic composition endmember with no salt intermixed. LOD2 corresponds to the concentration where the signal of the anion line is 2× the standard deviation of the blank above the signal in the blank. The signal from the blank can often be assumed to be close to zero; however, this is not the case for carbon, which is present in all measurements due to the atmosphere. Therefore, when above zero, the *y* intercept of the calibration curve was taken as the signal in the blank. Due to difficulties in obtaining accurate statistics in the absence of an anion line signal, the standard deviation used for this calculation was that of the lowest measured salt concentration. The factor of 2 determines the probability of obtaining false positives, corresponding to a 95% confidence interval. The third and final method determines the limit of quantification (LOD3) taking into account the 95% confidence interval of the calibration curve [*Massart et al.*, 1998, chap. 13]. This limit is included for consistency with previous ChemCam studies but is not as meaningful in this work because it assumes linear calibration curves, which was demonstrated to not be the case here (see section 4.3). Consequently, the limit increases with nonlinearity.

3. Results

3.1. Whole Spectrum Trends With Salt Concentration: Systematic Change in Continuum

The emission lines present for a given mixture are the same between samples of given salt concentrations, as analyzed further below and as expected. However, comparison of the single-shot spectra revealed—in addition to random effects due to the composition of individual grains hit and fluctuations in the laser power or experimental environment between shots—systematic changes with shot number that appear to be correlated with salt content. Over consecutive laser shots at a particular location, in a sample with a set salt concentration, the continuum emission generally increases with shot number for salt-bearing samples. More interestingly, the amount by which the continuum emission increases over the 50 laser shots seems to depend on the salt content. As shown for NaCl + K1919, the continuum increase per shot is greater for mixtures with higher salt concentrations, creating a larger spread in intensity from the first to the final laser pulse. In contrast, the basalt samples show very little continuum increase with shot number (Figure 3). Following continuum removal, no consistent whole-spectrum trends with shot number are observed.

3.2. Spectral Line Analysis

3.2.1. Salt Anion Emission Lines Detected in Mixtures

Spectra averaged over many laser shots show the most sensitive anion lines in basaltic mixtures, particularly after removal of the local continuum. Table 3 lists the Cl, C, and S lines that met the initial four

Table 3. Cl, C, and S Lines That Met the Initial Four Criteria Listed in Section 2.3 for Univariate Analysis of Salt + Basalt Mixtures in This Work[a]

	Reference Data				Quantitative Analysis					
λ (nm)	Ionization Level	Spectral Window	Reference Database		LOD 1	LOD 2	LOD 3	Begins Monotonic Increase	Unreliable Behavior	Met All Criteria for All Mixes
Chlorine										
385.2	II	VIO	NIST	Na + KB	*0.213*	0.058	0.117	0.038		
				Ca + KB	*0.386*	0.140	0.185	0.134		
				Na + GB	*0.325*	0.123	0.204	0.222		
507.9	II	VNIR	Martian, NIST		0.121	0.136	0.133	0.019		
					0.134	0.223	0.110	0.020		
					0.127	*0.307*	0.333	0.002		
510.1	II	VNIR	Martian, NIST		0.121	0.145	0.152	0.019		
					0.134	0.117	0.110	0.020		
					0.041	*0.224*	0.328	0.002		
521.9	II	VNIR	Martian, NIST		0.121	0.049	0.147	0.038		✓
					0.134	0.060	0.090	0.041		
					0.127	0.071	0.243	0.022		
539.4	II	VNIR	Martian, NIST		0.121	0.065	0.182	0.121		✓
					0.134	0.144	0.135	0.020		
					0.127	0.164	0.160	0.022		
542.5	II	VNIR	Martian, NIST		0.038	0.039	0.147	0.019		✓
					0.134	0.036	0.074	0.041		
					0.127	0.029	0.169	0.022		
544.5	II	VNIR	Martian, NIST		0.019	0.049	0.155	0.019		✓
					0.134	0.049	0.100	0.020		
					0.127	0.052	0.217	0.222		
545.9	II	VNIR	Martian, NIST		0.121	0.074	0.155	0.038		
					0.134	0.128	0.192	*0.386*		
					0.127	0.062	0.241	0.222		
725.9	I	VNIR	NIST		0.121	0.101	0.101	0.038		✓
					0.134	0.164	0.105	0.020		
					0.127	0.076	0.147	0.020		
741.6	I	VNIR	NIST		0.019	0.047	0.262	0.121	X	
					0.134	*0.275*	0.255	0.247		
					0.002	*0.337*	0.299	0.222		
754.9	I	VNIR	NIST		0.121	0.023	0.115	0.038		✓
					0.134	0.045	0.082	0.041		
					0.127	0.036	0.159	0.041		
771.9	I	VNIR	Martian, NIST		0.121	0.161	0.224	0.019		
					0.134	0.035	0.125	0.020		
					0.325	0.134	0.350	0.002		
774.7	I	VNIR	NIST		0.121	0.053	0.132	0.038		✓
					0.134	0.034	0.083	0.020		
					0.127	0.166	0.229	0.002		
809.1	I	VNIR	NIST		0.019	0.027	0.095	0.019		✓
					0.020	0.003	0.137	0.041		
					0.041	0.103	0.191	0.002		
833.6	I	VNIR	NIST		0.121	0.020	0.102	0.038		✓
					0.134	0.037	0.053	0.041		
					0.127	0.036	0.151	0.020		
837.8	I	VNIR	Martian, NIST		0.019	0.035	0.097	0.038		✓
					0.020	0.017	0.105	0.020		
					0.041	0.078	0.148	0.002		

Table 3. (continued)

Reference Data					Quantitative Analysis					
λ (nm)	Ionization Level	Spectral Window	Reference Database		LOD 1	LOD 2	LOD 3	Begins Monotonic Increase	Unreliable Behavior	Met All Criteria for All Mixes
Sulfur										
543.0, 543.4	II	VNIR	Martian, NIST	Ca + KB	0.016	0.021	0.050	0.008		✓
				Ca + GB	0.001	0.042	0.099	0.084		
				Mg + KB	0.001	0.031	0.042	0.053		
				Fe + KB	0.001	0.009	0.015	0.016		
				Na + KB	0.001	0.009	0.043	0.045		
545.5	II	VNIR	Martian, NIST		0.049	0.011	0.056	0.016		✓
					0.051	0.011	0.078	0.051		
					0.053	0.018	0.046	0.053		
					0.016	0.004	0.014	0.016		
					0.045	0.005	0.044	0.045		
Carbon										
247.9	I	UV	Martian, NIST	Ca + KB		0.083	0.076	X		
				Mg + KB		*0.217*	0.121	0.025		
283.8	II	UV	Martian, NIST			0.035	0.067	X		
						0.117	0.079	0.025		
657.9	II	VNIR	Martian, NIST			0.014	0.065	0.064		✓
						0.045	0.082	0.025		
678.6	II	VNIR	Martian, NIST		Detected in atmosphere in all samples	0.031	0.060	0.064		✓
						0.046	0.099	0.025		
711.8	I/II	VNIR	Martian, NIST			0.072	0.053	0.064		
						0.137	0.126	0.025		
723.8	II	VNIR	Martian, NIST			0.009	0.065	0.064		✓
						0.043	0.090	0.025		
833.7	I	VNIR	NIST			0.002	0.070	0.064		✓
						0.060	0.110	0.025		

[a]The reference wavelength values in vacuum, ionization level, and corresponding ChemCam detector spectral window are listed. The references are the Martian database of *Cousin et al*. [2011] and NIST spectral line database as described in the text. The remaining columns provide the results of this analysis: the detection limits determined based on the methods described in section 2.5, the concentration at which a monotonically increasing trend in peak area with salt concentration began (or an "X" if the peak area did not monotonically increase), and whether the peak area displayed unreliable behavior among the mixture compositions tested. Detection limits and concentrations are provided in mole fraction of element (χ) for each cation + basalt mixture combination. Italicized values are above 50 wt % salt. Mixtures in bold included an extra low concentration of 0.5 wt % salt (see section 2.1). A check mark in the final column indicates that the line met all seven criteria listed in section 2.3 for all mixture compositions tested and may be among the most effective for quantitative analysis. Calculated LOD1 is the lowest concentration measured for all carbonate-bearing mixtures (a mole fraction of 0.011 for Ca + KB and 0.001 for Mg + KB), but this results from atmospheric CO_2 rather than sample carbon.

criteria for identification described in section 2.3 and for which peak areas were measured in the salt + basalt mixtures. The anion line intensities are 1–3 orders of magnitude lower than those of the strongest elemental lines. Therefore, emission line overlap prevents many anion lines from being detected. The identified lines are spread across the 240–850 nm detectable wavelength range although most fall within the spectral range of the VNIR detector (470–850 nm). Relative to the VNIR, the spectral ranges of the UV and VIO detectors are smaller and contain many strong lines from cation and basaltic matrix elements. Peak centers do not always coincide with the exact line location listed in the NIST database. However, the peak identity has been determined based on the criteria described in section 2.3.

3.2.1.1. Cl Lines

Sixteen potential Cl lines are observed in the spectra of the chloride salt + basalt mixtures that met the initial criteria provided in section 2.3 (Table 3 and Figures 4, 5, and S3). Of the 16 selected lines, one appears in the range of the VIO detector, whereas the rest are in the VNIR. The nine lines at wavelengths shorter than 546 nm result from transitions of singly ionized Cl, whereas those above 725 nm are from neutral Cl.

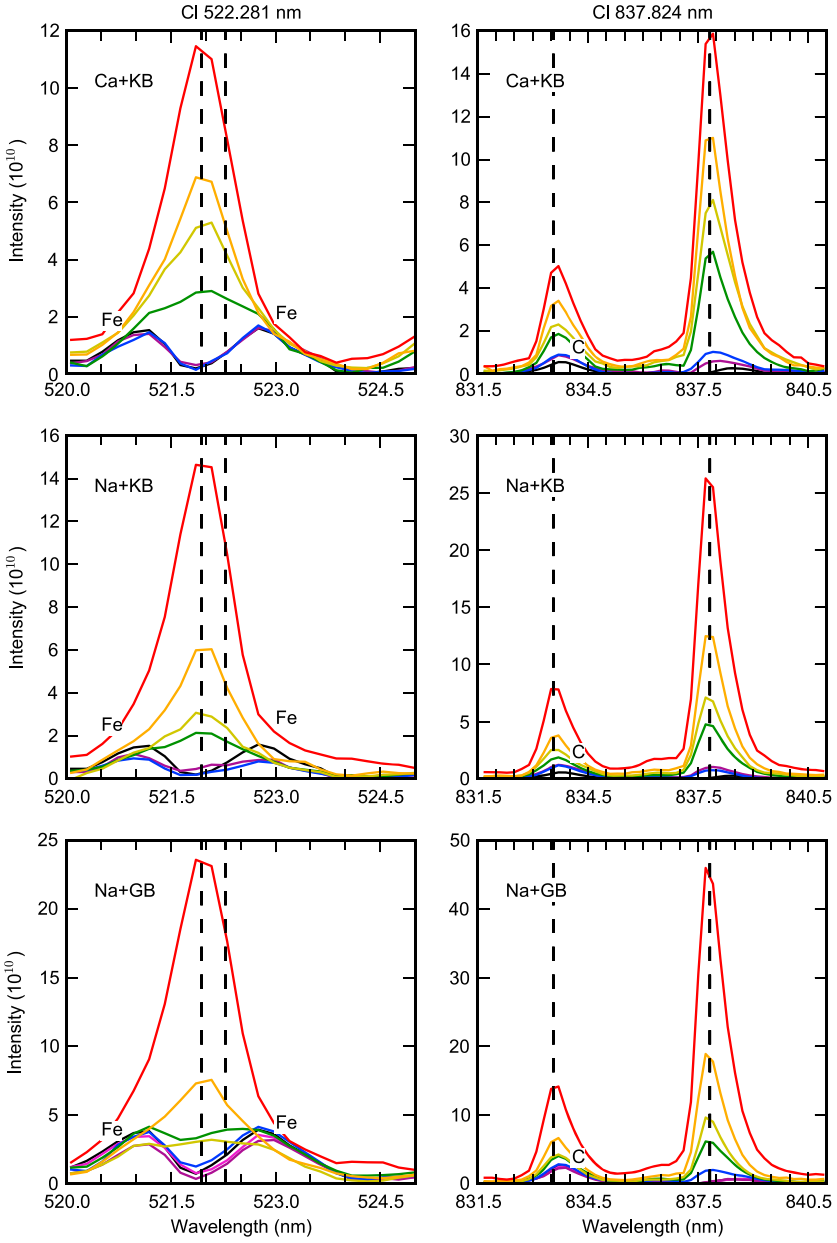

Figure 4. Spectra of Cl emission lines, denoted by vertical lines, at (left column) 521.9 nm and (right column) 837.8 nm in (top row) $CaCl_2$ + K1919 (Ca + KB), (middle row) NaCl + K1919 (Na + KB), and (bottom row) NaCl + GBW07105 (Na + GB) mixtures. Colors in the overlain spectra indicate different salt concentrations with pure basalt in black and pure salt in red, and mixtures containing salt mass fractions of 0.5 wt % (select mixtures only) in magenta, 5 wt % in purple, 10 wt % in blue, 30 wt % in green, 50 wt % in yellow, and 70 wt % in orange. Intensity is in units of photons/shot/mm^2/sr/nm. Spectra for all Cl lines are provided in Figure S3 in the supporting information.

The selected Cl lines are detectable despite some interference due to other elements in the sample. The outer tails of strong elemental lines can contribute emission to Cl peaks even a few nanometers away (e.g., an O peak at 777.6 nm affects the Cl peaks at 771.9 and 774.7 nm). Cl peaks are detected on the shoulder of some less intense lines (e.g., Cl at 725.9 nm appears on the outer tail of the C line at 723.8 nm) and blended with lines of comparable intensity (e.g., Cl at 507.9 and 510.1 nm; 544.5 and 545.9 nm). Weak emission features due to other elements appear within a few tenths of a nanometer of the Cl peak centers, but Cl emission appears to dominate the line location at high salt concentrations above LOD1 (Figure 4). Most selected Cl peaks show a monotonic increase in peak area for concentrations above 5–10 wt % salt (χ_{Cl} = 0.019–0.041; Table 3).

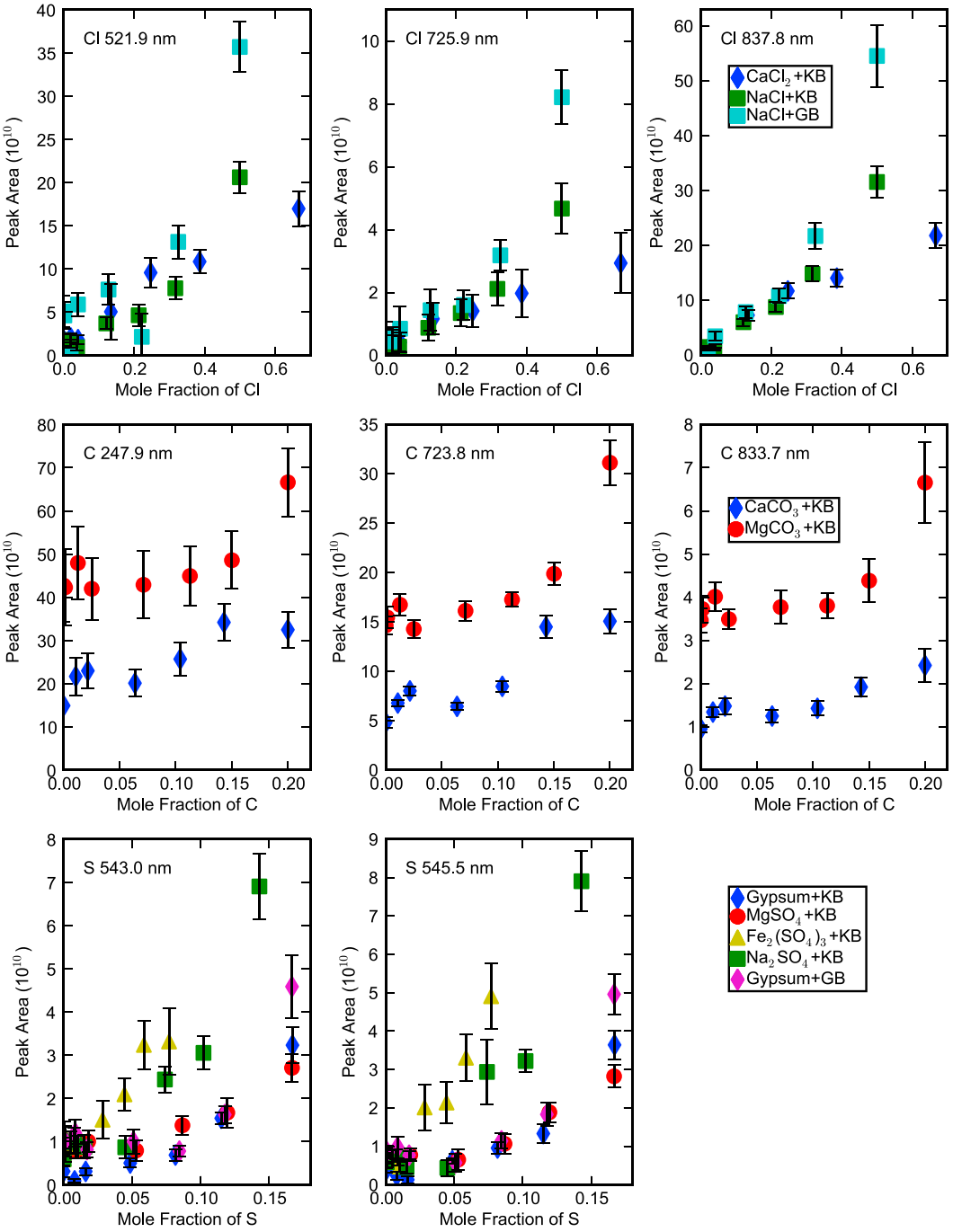

Figure 5. Calibration curves of peak area versus mole fraction of element for a selection of Cl, C, and S peaks and each salt + basalt combination (provided in the legend for each row). Peak areas are in units of photons/shot/mm^2/sr. Calibration curves for remaining Cl and C lines are provided in Figures S3 and S4 in the supporting information.

The NaCl + GBW07105 composition series, including the pure salt, tends to have comparable or larger Cl peak areas than that of NaCl + K1919 in the unnormalized data with exceptions at 507.9, 510.1, and 521.9 nm. A few Cl lines differ in appearance (e.g., 741.6 and 809.1 nm) and peak area trends (e.g., 507.9, 510.1, 741.6, and 809.1 nm) between the $CaCl_2$- and NaCl-bearing mixtures. The distinct behavior of the line at 741.6 nm between different mixtures calls into question the usefulness of this line. Peak areas of the remaining Cl lines are comparable between the $CaCl_2$- and NaCl-bearing mixtures until concentrations reach $\chi_{Cl} = 0.247–0.386$ (50–70 wt % $CaCl_2$) where the calibration curves diverge.

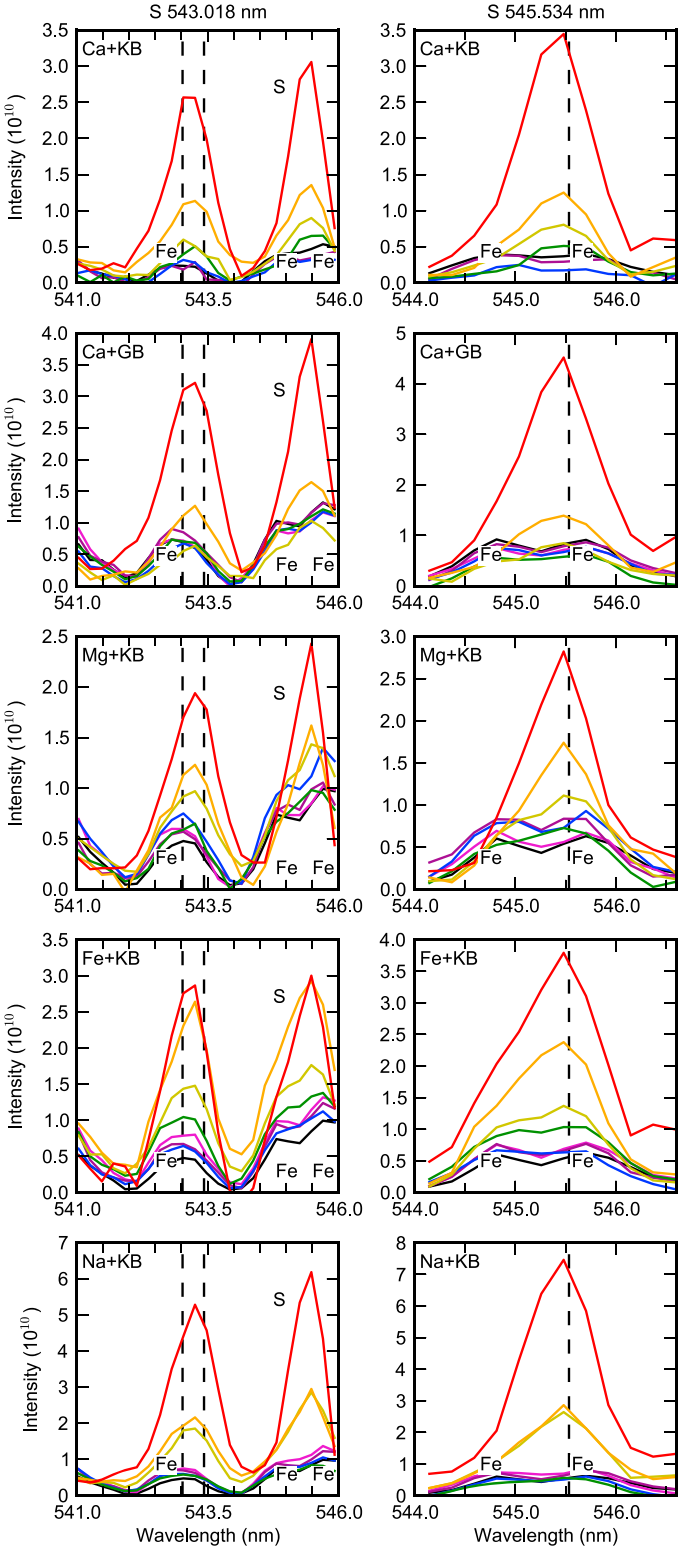

Figure 6. Spectra of S emission lines, denoted by vertical lines, at (left column) 543.0 nm and (right column) 545.5 nm in (first row) $CaSO_4 \cdot 2H_2O$ + K1919 (Ca + KB) and (second row) GBW07105 (Ca + GB), (third row) $MgSO_4$ + K1919 (Mg + KB), (fourth row) $Fe_2(SO_4)_3$ + K1919 (Fe + KB), and (fifth row) Na_2SO_4 + K1919 (Na + KB) mixtures. Colors in the overlain spectra indicate different salt concentrations with pure basalt in black, pure salt in red, and mixtures containing salt mass fractions of 0.5 wt % (select mixtures only) in magenta, 5 wt % in purple, 10 wt % in blue, 30 wt % in green, 50 wt % in yellow, and 70 wt % in orange. Intensity is in units of photons/shot/mm^2/sr/nm.

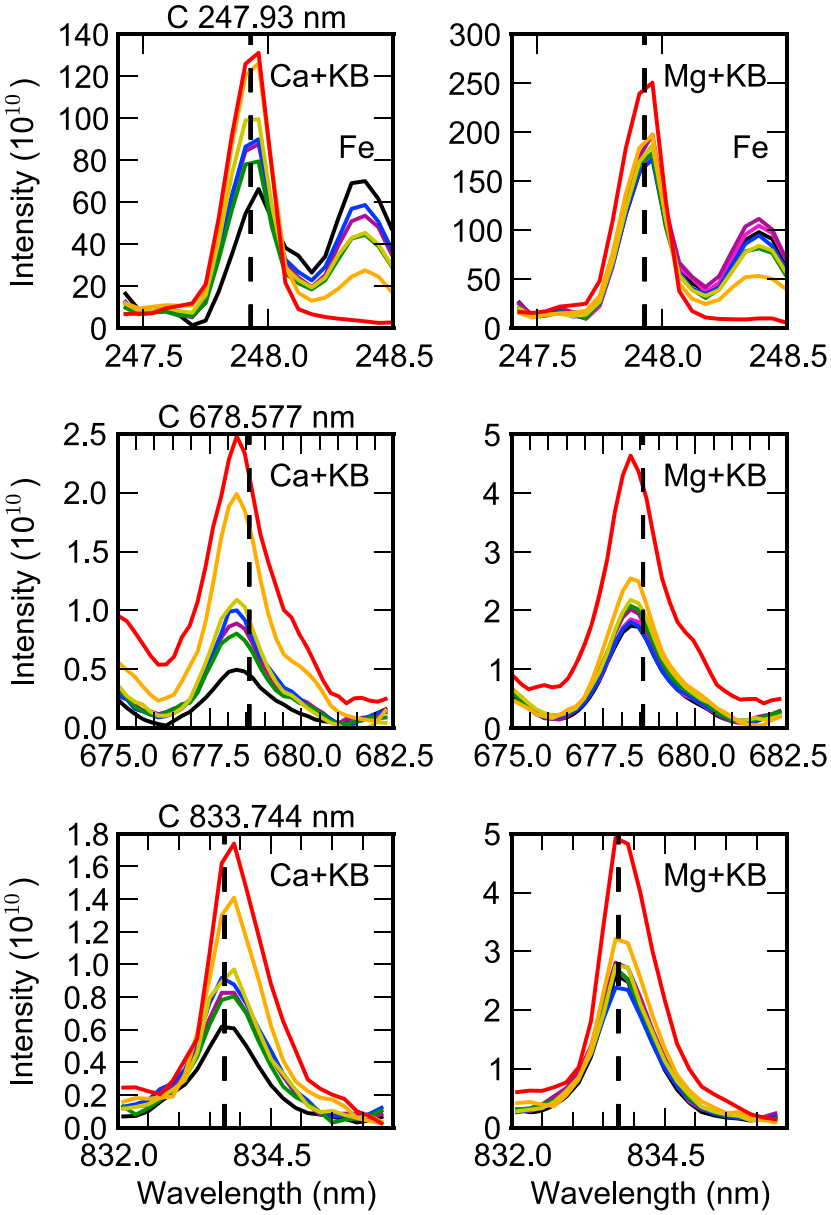

Figure 7. Spectra of C emission lines, denoted by vertical lines, at (top row) 247.9 nm, (middle row) 678.6 nm, and (bottom row) 833.7 nm in (left column) $CaCO_3$ + K1919 (Ca + KB) and (right column) $MgCO_3$ + K1919 (Mg + KB) mixtures. Colors in the overlain spectra indicate different salt concentrations with pure basalt in black, pure salt in red, and mixtures containing salt mass fractions of 0.5 wt % (select mixtures only) in magenta, 5 wt % in purple, 10 wt % in blue, 30 wt % in green, 50 wt % in yellow, and 70 wt % in orange. Intensity is in units of photons/shot/mm^2/sr/nm. Spectra for all C lines are provided in Figure S4 in the supporting information.

3.2.1.2. S Lines

The two sulfur peaks identified are part of a series that appear between 540 and 565 nm. This is the same region recommended by *Dyar et al.* [2011] for identification of sulfur in geologic samples and used by *Nachon et al.* [2014] for the identification of calcium sulfate veins by ChemCam in Gale crater. Peaks appear in this spectral region at high salt concentrations for all five of the sulfate + basalt mixtures investigated (Figures 5 and 6). However, a large number of spectral lines populate this region, particularly Fe and a few Ca lines, complicating the determination of individual peak areas. Fe lines within the range of the spectral resolution from both identified S peaks could not be definitively separated out. The influence of Fe emission on the peak shape and the concentration at which S begins to dominate, which can be seen for the 545.5 nm line in Figure 6, depends on the sample composition.

Measured peak areas increase monotonically with salt concentration above 10–30 wt % salt ($\chi_S = 0.045$–0.053) for all mixtures with the exception of gypsum + GBW07105 at 543.0–543.4 nm from 30 to 50 wt % salt ($\chi_S = 0.051$–0.084). In the case of gypsum + K1919, the area of the peak at 543.0–543.4 nm increases monotonically for all concentrations. Gypsum- and $MgSO_4$-bearing mixtures have comparable peak areas at each salt concentration in the unnormalized data, whereas the $Fe_2(SO_4)_3$- and $NaSO_4$-bearing mixtures have higher values. Peak areas differ for the pure salts, including the two gypsum measurements taken on different experimental setups (see section 2.1).

3.2.1.3. C Lines

Detection of carbon is more complicated than that of Cl or S because the abundance of CO_2 in the Martian atmosphere can cause C lines to appear in the LIBS spectrum. The LIBS laser does not excite the ambient gas, but when a plasma is created by laser interaction on a solid target (soil, rock, or pressed pellets), the atmospheric constituents are also excited due to partial breakdown of the gas just over the sample surface. As such, the C peaks identified in the spectra of carbonate-bearing samples were also found in the spectra of other samples that did not contain appreciable carbon.

Seven potential C lines are identified in the carbonate + basalt mixtures that met the initial four criteria from section 2.3 (listed in Table 3). Two appear in the UV spectral window and five in the VNIR (Figures 5, 7, and S4). The transitions are mainly from singly ionized C with 2–3 from neutral C. Some of the selected lines partially overlap with emission from other elements, but this does not inhibit identification of the C line. The C lines at 247.9 and 283.8 nm experience interference due to Fe only in the presence of the basaltic matrix. The C line at 657.8 nm blends with the H line at 656.5 nm in the $MgCO_3$-bearing samples but has little to no influence from the H line in $CaCO_3$-bearing samples. Although not clearly visible here, there may also be interference from Fe and Ti in this H/C line region [*Schröder et al*., 2015; *Rapin et al*., 2016]. Ca at 715.0 nm interferes with the C line at 711.8 nm in all $CaCO_3$- and $MgCO_3$-bearing samples.

Peak areas monotonically increase for concentrations above 10–30 wt % salt ($\chi_C = 0.025$–0.064) with the exception of the lines at 247.9 and 283.8 nm in $CaCO_3$ + K1919. The $MgCO_3$ + K1919 composition series generally displays higher peak areas in the unnormalized data and different trends in the calibration curves compared to the $CaCO_3$ + K1919. The change in sample-to-target distance between the mixture series likely contributed to these differences as described in section 4.2. Lines show weak sensitivity to concentration from 30 to 70 wt % $MgCO_3$ ($\chi_C = 0.071$–0.150) and from 70 wt % to pure $CaCO_3$ ($\chi_C = 0.143$–0.200) for some C peaks.

3.2.2. Limits of Detection for Salt Anion Elements

The detection limits depend on both the line selected and the mixture composition (Table 3). Based on LOD1, Cl is detectable via most lines at 30 wt % salt, equal to a mole fraction of $\chi_{Cl} = 0.12$–0.14 or about 18–19 wt % Cl. However, a few Cl lines can be detected down to 5–10 wt % salt, equal to $\chi_{Cl} = 0.02$–0.04 or 3–6 wt % Cl. LOD2 gives a comparable range of $\chi_{Cl} = 0.02$–0.17 with exceptions at 507.9, 510.1, 741.6, and 809.1 nm. The S line at 543.0–543.4 nm is detected (LOD1) at 0.5 wt % salt ($\chi_S = 0.001$, 0.1 wt % S) except in gypsum + K1919 where it is detected only above 10 wt % ($\chi_S = 0.016$, 2 wt % S). LOD2 produces higher values of $\chi_S = 0.009$–0.042 (~5–25 wt % salt, 1–6 wt % S). The S line at 545.5 nm is detected (LOD1) at 30 wt % salt ($\chi_S = 0.034$–0.053, 7–8 wt % S) in all mixtures except $Fe_2(SO_4)_3$ + K1919. LOD2 produces lower values of $\chi_S = 0.004$–0.018 (~3–10 wt % salt, 0.7–3 wt % S). For C, the limit of detection analysis is affected by carbon present in the CO_2 atmosphere. As a result, carbon emission is detected at all concentrations even in the blank and LOD1 does not provide any extra information (see note in Table 3). LOD2 is the meaningful limit in this case. C lines at 657.9, 678.6, 723.8, and 833.7 nm have detection limits $\chi_C = 0.04$–0.06 (~20–25 wt % salt, 2–4 wt % C) in $MgCO_3$ + K1919 with lower values in $CaCO_3$ + K1919 (~1–15 wt % salt, 0.1–2 wt % C). The remaining lines have higher detection limits, >35 wt % salt, with the exception of 283.8 nm in $CaCO_3$ + K1919 (~15 wt % salt, 2 wt % C).

4. Discussion

4.1. Detection of Salt Anions

Table 3 summarizes the results of the quantitative analysis. Ten Cl lines met our complete criteria for being useful for quantitative analysis of chloride + basalt mixtures. Chlorides were detectable at ~5–10 wt % in

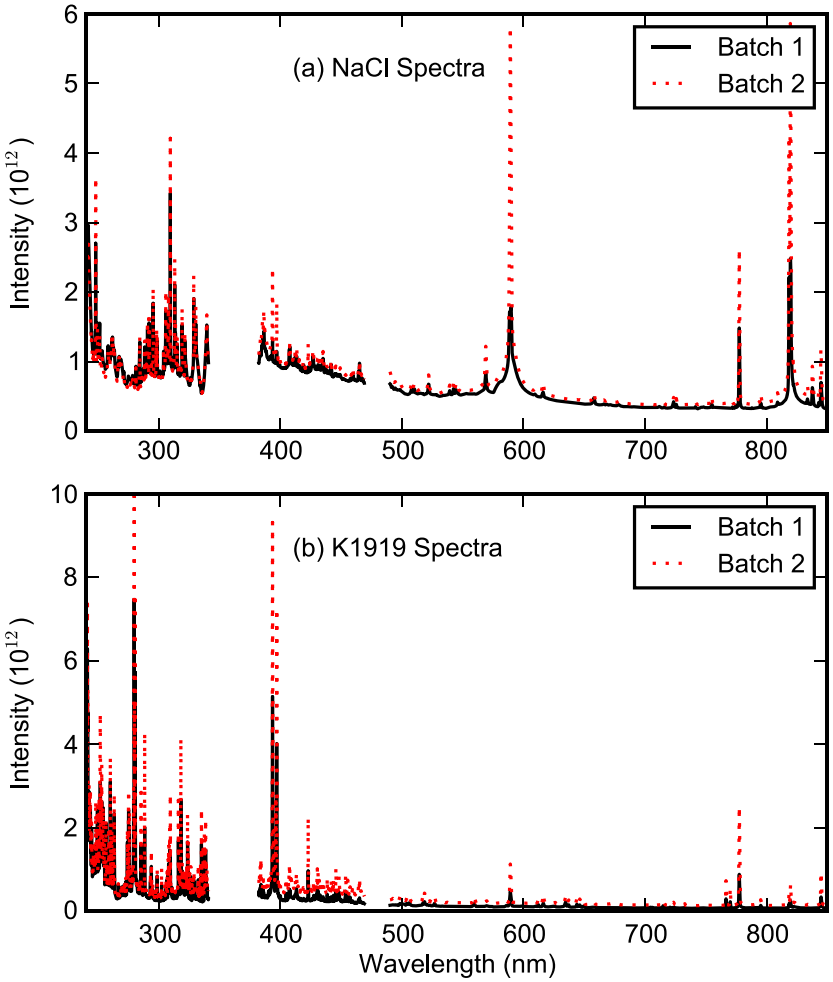

Figure 8. Comparison of (a) NaCl and (b) K1919 spectra collected in the first (solid black line) and second batches (dotted red line) of measurements at laser-to-sample distances of 1.6 and 3.0 m, respectively, after processing to correct for the geometric effects of distance.

the basaltic background using select lines. The line at 837.8 nm appears to be the most promising for quantification with this univariate method based on its low detection limit, sensitivity to concentration, and reliable behavior in all mixture compositions. Of the detected Cl lines, this line also has the lowest upper state energy and a relatively high transition probability (Einstein A coefficient) based on values from the NIST database [*Kramida et al*., 2015].

Interference from Fe emission complicates the detection of S. Due to the broadness of the peak spanning Fe at 542.9 nm and individual S transitions at 543.0 and 543.4 nm, it is difficult to eliminate Fe interference by tracking changes in the peak center with salt concentration. Therefore, the LOD2 values seem more appropriate for this S peak. Given this consideration, sulfates are detected in the basaltic background at 5–30 wt % salt (LOD1 at 545.5 nm) but could be detectable at as low as 3–10 wt % based on LOD2. Even still, it will be difficult to distinguish Fe from S emission in the spectra. Quantification based on the S lines at 543.0/543.4 and 545.5 nm will require knowledge about the Fe content of the target due to almost direct overlap with Fe peaks in the spectral region. However, the Fe content can be measured relatively easily using the multitude of strong Fe lines present throughout the ChemCam spectral range.

Carbonates are detectable in excess of the carbon emission due to the atmosphere at ~20 wt % in the basaltic background for either salt tested and potentially down to 1 wt % salt for $CaCO_3$. The overall detection limit is similar to the value of 6 wt % C determined by *Ollila et al*. [2013] for a set of geologic samples and 5 wt % C by *Beck et al*. [2016] for $CaCO_3$ + basalt mixtures but appears lower for certain lines in $CaCO_3$ + K1919. Precise

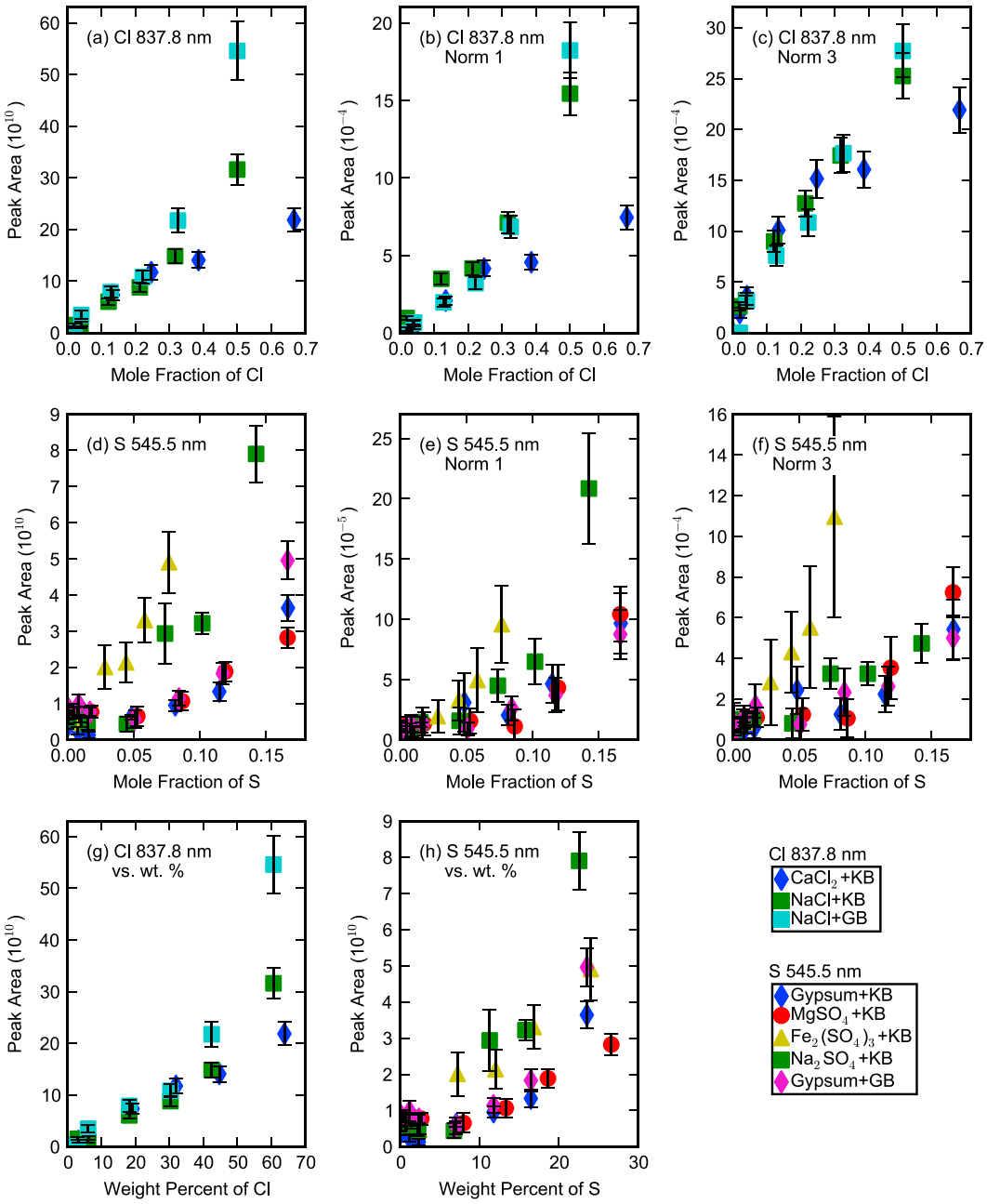

Figure 9. Calibration curves for (a–c and g) Cl at 837.8 nm in NaCl + K1919, $CaCl_2$ + K1919, and NaCl + GBW07105 and (d–f and h) S at 545.5 nm in $Fe_2(SO_4)_3$ + K1919, Na_2SO_4 + K1919, $MgSO_4$ + K1919, gypsum + K1919, and gypsum + GBW07105 plotting unnormalized peak area versus mole fraction of element (Figures 9a and 9d), peak area normalized by the total spectral emission across the entire spectral wavelength range (Figures 9b and 9e), peak area normalized by the total spectral emission of the VNIR detector wavelength range (Figures 9c and 9f), and unnormalized peak area versus weight percent of element (Figures 9g and 9h). Peak areas are in units of photons/shot/mm^2/sr.

quantification based on the lines selected here may be difficult because their areas lack sensitivity to changes in concentration from 30 to 70 or 70 to 100 wt % salt depending on mixture composition.

Cl and S peaks are both present in the 540–548 nm range; however, these peaks can be distinguished by slight differences in the location of the peak center in addition to peak shape. Cl peaks at 542.5, 544.5, and 545.9 nm are visible in all three chloride salt + basalt mixtures, and the 544.5 and 545.9 nm peak emission overlaps strongly creating a distinct shape compared to the two S peaks at 543.0/543.4 and 545.5 nm. Additionally, the fourth Cl peak at 539.4 nm can distinguish the presence of Cl. Another potential conflict

in identification occurs between the Cl peak at 833.6 nm and the C peak at 833.7 nm. The Cl peak has a peak area 2–4× larger than the C peak at high salt concentrations and has a lower detection limit. To eliminate confusion, several of the stronger Cl lines including one nearby at 837.8 nm could indicate the presence of Cl.

4.2. Effects of Basaltic Matrix and Salt Cation on Anion Lines

The basaltic matrix and/or salt cations affect the appearance and behavior of some of the selected anion peaks. The detection limits also varied with mixture composition for these lines. For example, all selected C lines had higher LOD2 values in $MgCO_3$ + K1919 than in $CaCO_3$ + K1919. Several lines met all seven criteria from section 2.3 and were found useful for analysis regardless of sample composition (see Table 3). However, even for these lines, the intensities and the behavior of the calibration curves were not uniform for all mixtures.

Anion peak areas differed between some mixtures with identical salt content but different matrix compositions (moderate- versus high-alkali basalt). However, the peak areas for the *pure salts* also differed between the two sets of measurements. This suggests that at least some, if not all, of the differences are due to factors unrelated to the composition of the matrix. Alteration to the experimental setup, in particular the laser-to-sample distance, between the first and second batches of measurements is observed in the comparison between distance-corrected, processed spectra of pure NaCl and K1919 samples measured in each batch (Figure 8). The spectra share the same emission lines, but the data collected at a laser-to-sample distance of 3.0 m have larger intensities than those collected at 1.6 m. The differences in absolute line intensity therefore cannot be attributed to the composition of the matrix alone as the sample distance likely has a significant effect on this quantity, even after correcting for solely geometric effects.

Differences in total emission produced by the sample were accounted for through normalization of key Cl and S lines (Figure 9). Such normalization appears to reduce effects on the calibration curve caused by the composition of the matrix or experimental setup based on comparison between the two different NaCl and gypsum composition series. However, the calibration curves maintain some dependence on the identity of the salt cation despite normalization. Divergence of the calibration curves appears at high salt concentrations, above 50 wt % chloride and above 30–50 wt % sulfate. Therefore, the composition of the sample, at least the salt cation, will have an effect on quantification of the anion elements.

4.3. Univariate Analysis of Salt Anion Elements

The peak areas of select anion lines increased monotonically above the detection threshold of the line (see Table 3). Therefore, univariate analysis could be useful in tracking relative changes in salt content given a sufficient abundance of salt. However, absolute quantification of salts in unknown samples would be difficult with univariate analysis. Relating the line area to an absolute element or salt concentration relies on comparison with laboratory data collected on known standards under similar experimental conditions. The shape of the calibration curve for a given emission line as a function of mole fraction depends on the composition of the sample even after normalization of the peak areas (Figure 9). This makes absolute measurements of elemental composition based on univariate analysis unreliable without prior knowledge of the sample composition, in particular the salt cation element. If trends were more similar as a function of weight percent, this might suggest a relationship with the mass of the atoms rather than the total number of emitting atoms, e.g., due to the extra energy required to eject more massive elements from the sample surface resulting in a concentration of these elements at the surface. However, it is not clear that this is the case here (Figures 9g and 9h).

The primary goal of this work is to identify the most suitable anion lines for detection and quantification. A next step is to apply this knowledge to the Mars data set. Developing quantitative calibration curves for the Mars data is beyond the scope of this work. It requires further investigation to correct for laser-to-target distance and laboratory-to-Mars instrument differences. In addition, there are challenges regarding univariate analysis itself. Finding the correct functional form to describe the calibration curves is also a question, even for the relatively well-behaved Cl line at 837.8 nm (Figure 10). For a given peak area of 7×10^{10} photons/shot/mm^2/sr, the estimated mole fraction of Cl can vary from 0.14 to 0.19 (~19–25 wt % Cl or 30–40 wt % salt) for a single composition, depending on whether the fit is linear, exponential or a power law (Figure 10). The uncertainty increases with increasing salt content and for a target with unknown composition. While normalization appears to increase the linearity of some curves, it does not have the same effect

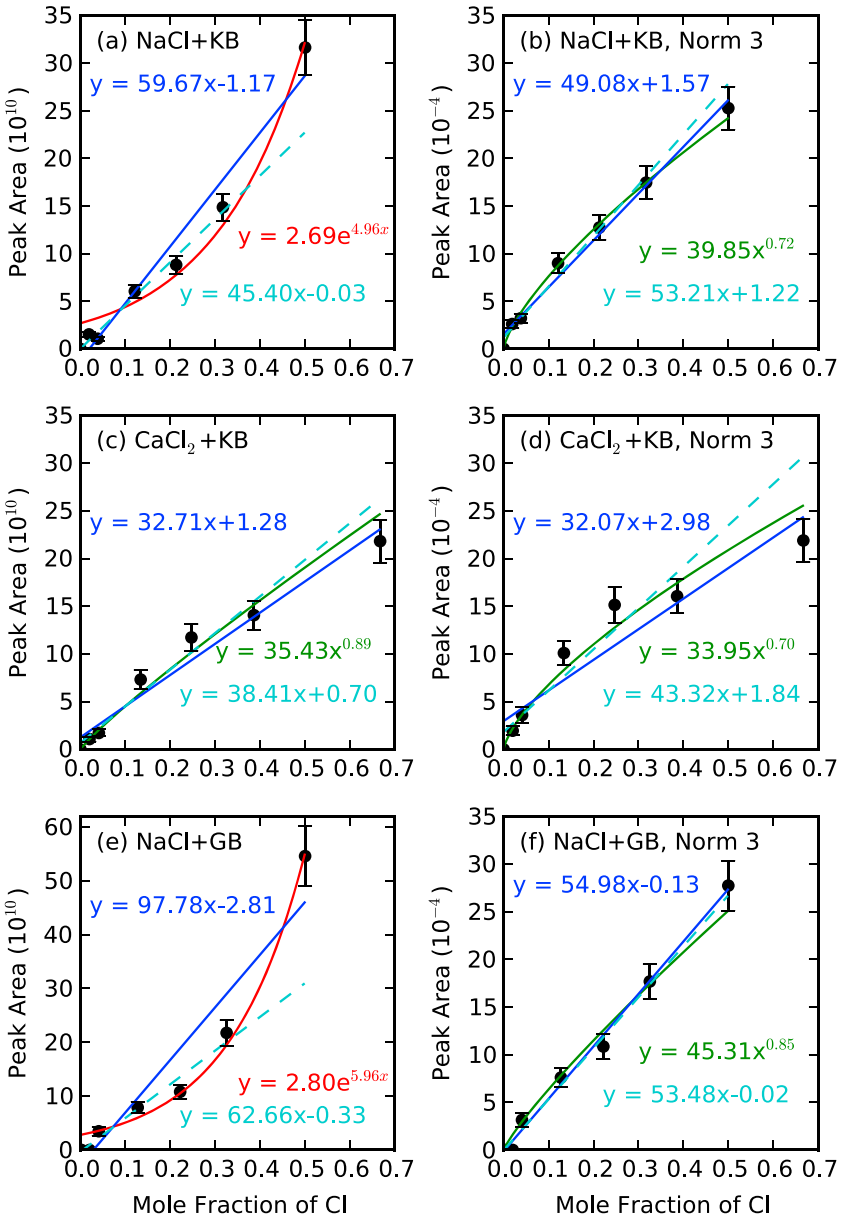

Figure 10. Potential fits to calibration curves for Cl at 837.8 nm in (a and b) NaCl + K1919, (c and d) $CaCl_2$ + K1919, and (e and f) NaCl + GBW07105 unnormalized (Figures 10a, 10c, and 10e) and normalized by the total intensity of the VNIR spectral window (Figures 10b, 10d, and 10f). The blue line is a linear fit to all data points, the cyan line is a linear fit to all data points excluding the pure salt, the red curve is an exponential fit, and the green curve is a power law fit to all data points. Peak areas are in units of photons/shot/mm^2/sr.

on all lines or compositions (Figures 10b and 10f versus Figure 10d). We provide all of the data necessary to recreate the calibration curves in the supporting information so that the interested reader may investigate further the application to ChemCam or other data sets.

4.4. Comparison to Prior Laboratory LIBS Studies of Cl, C, and S: Most Effective Lines for Analysis

Previous studies focused on the identification of Cl, C, and S emission with ChemCam tested a range of samples from pure compounds to geologic materials (see section 1). The salt + basalt mixture spectra evaluated here are complex, thus challenging observation of key emission lines. The large number of emission lines and additional matrix effects, potentially including preferential recombination of elements of interest from the bulk basalt-containing mixture, increase the likelihood of nondetection of lines due to

Table 4. Cl Emission Lines Identified as Being Useful for Identification of These Elements in Salt + Basalt Mixtures According to the Specific Criteria Applied in This Work Described in Section 2.3 ("✓" for All Seven Criteria, "-" for Only Initial Four Criteria)[a]

	Chlorine					
λ (nm)	$CaCl_2$ (K1919)	NaCl (K1919)	NaCl (GBW)	Cousin et al.	Schröder et al.	All Sources
299.8				✓		
310.5				✓		
385.2	-	-	-		✓	
386.1					✓	
413.4				✓		
422.8				✓		
426.6				✓		
460.9				✓		
479.6					✓	
481.1					✓	
482.0					✓	
489.8					✓	
507.9	✓	✓	-	✓		
510.1	✓	✓	-	✓		
521.9 (2), 522.3	✓	✓	✓	✓	✓	✓
539.4	✓	✓	✓	✓	✓	✓
542.5 (2)	✓	✓	✓	✓	✓	✓
544.5 (2)	✓	✓	✓	✓	✓	✓
545.9 (2)	-	✓	✓	✓	✓	
611.6				✓		
614.2				✓		
684.2				✓		
693.5				✓		
725.9	✓	✓	✓			
741.6	-	-	-			
754.9	✓	✓	✓			
771.9	✓	✓	-	✓		
774.7	✓	✓	✓			
798.3				✓		
809.1	✓	✓	✓			
833.6	✓	✓	✓		✓	
837.8	✓	✓	✓	✓	✓	✓
839.4				✓		
840.9				✓		
843.0					✓	

[a]To elucidate effects due to the matrix, lines selected in previous studies of pure elements or compounds by *Cousin et al.* [2011], *Schröder et al.* [2013], and *Ollila et al.* [2011] are provided for comparison. A check mark in the final column indicates that the peak was selected as useful for analysis in all observed sources in this work and the literature. Parentheses following the wavelengths indicate the number of lines at that position that may be unresolved in some cases.

Table 5. For S Lines, Equivalent to Table 4

	Sulfur							
λ (nm)	$CaSO_4$ (K1919)	$CaSO_4$ (GBW)	$MgSO_4$ (K1919)	$Fe_2(SO_4)_3$ (K1919)	Na_2SO_4 (K1919)	Cousin et al.	Schröder et al.	All Sources
330.3						✓		
334.8						✓		
386.0						✓		
402.9						✓		
403.4						✓		
414.3						✓		
415.4						✓		
416.3						✓		
417.5						✓		
440.6						✓		
445.2						✓		
446.6						✓		
455.3						✓		
468.3						✓		
534.7						✓		
536.4						✓		
543.0, 543.4	✓	✓	✓	✓	✓	✓	✓	✓
545.5	✓	✓	✓	✓	✓	✓	✓	✓
547.5							✓	
547.9						✓		
551.1							✓	
553.8						✓		
556.7							✓	
560.7							✓	
564.1							✓	
564.7							✓	
566.1							✓	
566.6						✓		
605.4						✓		
614.1						✓		
631.4						✓		
638.7						✓		
639.7						✓		
639.9 (2)						✓		

Table 6. For C Lines, Equivalent to Table 4

	Carbon				
λ (nm)	$CaCO_3$ (K1919)	$MgCO_3$ (K1919)	Cousin et al.	Ollila et al.	All Sources
247.9 (2)	-	-	✓	✓	
250.9			✓	✓	
251.3			✓	✓	
274.2			✓		
274.7			✓		
283.8 (2)	-	-	✓	✓	
298.3			✓		
299.3			✓	✓	
387.7 (3)				✓	
392.0 (2)				✓	
406.9			✓		
407.0			✓		
407.1			✓		
407.6			✓	✓	
407.7			✓	✓	
426.8 (2)			✓	✓	
432.7			✓		
464.9			✓		
465.2			✓		
465.3			✓		
466.7			✓		
505.4			✓		
513.4			✓		
513.5			✓		
514.5				✓	
514.7			✓	✓	
564.8				✓	
566.2				✓	
569.4				✓	
569.8			✓		
589.1 (2)			✓		
657.9	✓	✓	✓	✓	✓
658.5				✓	
658.9				✓	
678.6	✓	✓	✓	✓	✓
711.8 (5)	✓	-	✓	✓	

Table 6. (continued)

	Carbon				
λ (nm)	$CaCO_3$ (K1919)	$MgCO_3$ (K1919)	Cousin et al.	Ollila et al.	All Sources
723.3, 723.8 (2)	✓	✓	✓	✓	✓
833.7	✓	✓		✓	

interference. This causes fewer lines to be detected from anion elements in mixtures compared to those identified in the controlled laboratory compounds by *Cousin et al*. [2011]. *Cousin et al*. [2011] detected 27 transitions for Cl, 33 for C, and 28 for S of which only 9 Cl, 3 C, and 2 S lines met all our criteria for potential usefulness in analysis of the salt + basalt mixtures (not all of these were resolved as separate peaks). Unexpectedly, the C line at 883.7 nm and Cl lines at 725.9, 754.9, 774.7, 809.1, and 833.6 nm from the NIST database were detected and identified as useful in the salt + basalt mixtures but not previously by *Cousin et al*. [2011]. These differences in line detections may be due to the significantly improved spectrometers used for ChemCam.

The most effective lines for the analysis of unknown Martian materials will likely be those that appear consistently in samples with various chemical compositions. Compared to the number of identified lines in pure elements and compounds, those found in the salt + basalt mixtures are more limited. However, there are emission lines of Cl, C, and S that appeared across multiple samples and may be promising for use in geologic targets. Tables 4–6 provide a comparison of the lines selected in this study with those from the works of *Cousin et al*. [2011], *Ollila et al*. [2011], and *Schröder et al*. [2013]. The most reliable lines found in this work that may be useful for further analysis based on appearance in all tested samples here and in the literature are indicated in the final column of the table. For Cl, lines at 521.9, 539.4, 542.5, 544.5, and 837.8 nm have been identified in all sources listed here. All C lines selected here for the carbonate + basalt mixture sets were observed by *Cousin et al*. [2011] and *Ollila et al*. [2011] except for 833.7 nm. Our analysis of sulfate + basalt mixtures agrees with prior work by *Dyar et al*. [2011], *Sobron et al*. [2012], and *Schröder et al*. [2013] to focus on the 540–565 nm region for the identification of sulfur, in particular the 543.0, 543.4 (overlapping), and 545.5 lines while simultaneously evaluating the effects of contributing Fe lines at that location.

4.5. Analysis of Salts With ChemCam in Gale Crater

Nachon et al. [2014] detected sulfur in calcium sulfate veins crossing sedimentary deposits in Yellowknife Bay. These detections were made through the presence of S lines at 543.3, 545.4, and 547.4, and a doublet at 564.0 and 564.4 nm. The lines at 543.4 and 545.5 nm were selected for analysis in the salt + basalt mixtures. In contrast, the line at 547.5 nm only potentially appears in the Na_2SO_4 + K1919 mixtures at high salt concentrations. *Cousin et al*. [2011] identified a line at 547.9 but not at 547.5 nm. The 547.5 nm region suffers interference from a small peak at 547.9 nm potentially due to Ti and large Ca peaks at 558–562 nm. The doublet at 564.0 and 564.4 nm did not meet our criteria for selection given that it appeared in a noisy spectral region due to interference from multiple elements in the basaltic matrix. *Cousin et al*. [2011] did not identify this doublet either.

Forni et al. [2015] detected Cl in two Martian targets through molecular CaCl emission. Given the high abundance of Na detected in these Cl-bearing targets, it was suggested that the Cl may have been present in the form of NaCl with the CaCl emission resulting from recombination of Cl in the plasma with Ca released from other phases. Chlorine was detected at levels as low as 0.6 wt % in laboratory mixtures of $CaCO_3$ with $CaCl_2$ by *Gaft et al*. [2014] and 2.5 wt % in synthetic chlorapatite + basalt mixtures by *Meslin et al*. [2016], well below the limit observed here for the atomic Cl lines. However, the ability to detect Cl through molecular lines relies on the presence of sufficient calcium in the sample [*Vogt et al*., 2017], whereas the atomic line emission can appear independently. Here we only observed the CaCl molecular lines in the $CaCl_2$ + K1919 compositional series, not in the NaCl + basalt mixtures (see Figure S5). Work is ongoing to explore the detectability of perchlorates, which have been identified at Gale crater by the Sample Analysis at Mars (SAM) instrument [*Leshin et al*., 2013; *Ming et al*., 2014] and previously at the Phoenix landing site [*Hecht et al*., 2009], in LIBS spectra [*Schröder et al*., 2017].

ChemCam analyses of carbon in the Martian surface are underway, and preliminary reports have suggested detections [*Beck et al*., 2016]. These results use the intensity of the C line at 723.7 nm relative to the O line at 777.6 nm. In addition, *Rapin et al*. [2016] use the C line at 247.9 nm for normalization of hydrogen emission therefore relying on the stability of its line strength assuming a relatively constant abundance of carbon in the Martian CO_2 atmosphere. The 247.9 nm line was found to be rather insensitive to salt concentration with its peak area only significantly increased in the pure $MgCO_3$ sample, peak area decreasing from 70 to 100 wt % Ca CO_3, and a high detection limit. This suggests that the usage of this line for H normalization would only be affected by the composition of the rock target if the rock were majority carbonate.

4.6. Future Prospects for Salt Analysis on Mars With ChemCam and SuperCam

Applying these results to the study of the Martian surface is the ultimate goal of this work. Multiple emission lines of Cl, C, and S were found in the LIBS spectra despite the interference from the basaltic background. Many of these lines displayed sensitivity to salt concentration and could provide at least some quantitative information about the sample composition. Clear detection of all three elements could be made in the spectra at ~30 wt % salt with some emission lines providing even lower detection limits. Therefore, Cl, C, and S may be detectable in a porous sandstone mostly or completely filled with salt. Pore spaces can occupy 14–49% of the rock in sandstones [*McWorter and Sunada*, 1977]. This corresponds to rock compositions of about 11–43 wt % NaCl or 15–52 wt % $Fe_2(SO_4)_3$. Lower concentrations due to passing fluids coating grains or partially filling pore spaces may be detected for salts of certain compositions, which were found to have detection limits around 1–10 wt % salt for select lines. Selected element lines were found to increase monotonically with salt concentration above a given threshold (Table 3), potentially allowing for relative changes in salt concentration to be observed. However, the dependence of calibration curve trends on the salt cation-anion pairing, at least for high salt concentrations, hinders the ability to obtain absolute quantification of Cl, C, and S through direct comparison between laboratory samples and Martian targets of unknown composition. Differences between the moderate and high-alkali basalts were found to have little effect on the curves following normalization. Determination of the major element concentrations and identification of the salt cation may provide sufficient knowledge to make more accurate comparisons with the laboratory data. Although it is difficult due to their weak emission relative to that of the major elements, further work involving multivariate analysis of these elements or a multiline approach may be warranted. Ultimately, even with only the ability to track relative changes in salt concentration assuming a single salt present, ChemCam will still be capable of distinguishing evaporite and siliciclastic layers throughout its traverse for follow-up with Curiosity's in situ analysis instruments.

This work is likely to be useful for the Mars 2020 mission as well, for which LIBS will again be used, this time as part of the SuperCam instrument, which will have improved sensitivity and spectral resolution in the VNIR range. At the sulfur emission wavelengths (~545 nm) SuperCam is expected to have a factor of 2× better resolution (going from ~0.65 nm on ChemCam to ~0.30 nm full width at half maximum on SuperCam). This will aid in separating the S emission lines from the interfering lines that complicate the ChemCam spectra. The spectral resolution will also be improved at longer wavelengths, e.g., for C and Cl emission lines. SuperCam will use a temporally gated intensifier for this spectral range, providing capabilities to boost the signal at times, so that minor peaks can be more clearly observed. The time gating can also be used to temporally distinguish between peaks. SuperCam will also have the ability to corroborate LIBS elemental identifications with mineral signatures from remote Raman and visible and infrared reflectance spectroscopy.

4.7. Potential Value of the Continuum Emission for Detecting Salts

As discussed in section 3.1, the continuum intensity displayed systematic trends over multiple consecutive laser shots that correlated with the salt content of the sample. Increasing continuum intensity has been noted in LIBS analysis of solid materials where consecutive laser pulses are targeted at the same location on a sample [*Corsi et al*., 2005]. These trends are not found when analyzing gases [e.g., *Carranza and Hahn*, 2002], suggesting that the cause is due to interaction with the solid surface. The cause may be confinement of the plasma within the ablation pit that develops following subsequent laser pulses on a single location. By enclosing the plasma, the interaction between its component electrons, ions, and atoms is intensified producing more emission. The strength of this emission will increase as the pit becomes deeper and is proportional to the ablated mass. However, there may be competing effects including cooling of the plasma due to interaction with the walls of the pit [*Corsi et al*., 2005].

The cause for the larger increase in continuum intensity over consecutive laser shots in the salts and salt-rich mixtures relative to the basalts is not clear. This distinction is unlikely to be caused directly by the elemental composition of the sample but may be related to or correlated with the physical properties of the sample surface. Relevant properties may include the hardness or strength of the material, which would affect the total ablated mass, or the laser-to-sample coupling due to differences in albedo or optical constants. However, correlations have been previously noted between the total integrated continuum intensity and the abundance of elements Fe and Na [*Tucker et al*., 2010]. This could be the result of more efficient ionization of these elements resulting in higher electron densities in the plasma. Multiple hypotheses exist for the continuum behavior observed here, and future work is required to determine the cause. Such work may aid in devising additional methods for inferring the presence or tracking changes in abundance of salt in ChemCam targets with supporting elemental compositions. In conjunction with previous studies that have found the continuum to provide useful information or normalizations [e.g., *Tucker et al*., 2010; *Schröder et al*., 2015], this work suggests that the continuum emission warrants further consideration and may contribute diagnostic information particularly if included in multivariate LIBS analyses.

5. Conclusions

Weak anion lines of Cl, S, and C can be detected due to the presence of salt even among the large number of elemental lines and the matrix effects caused by a basaltic background. Of many more lines considered, a selection were evaluated using univariate analysis and 10 Cl, 4 C, and 2 S lines met all our criteria for potential usefulness in quantification. These results are promising for the detectability of diagenetic cements in basaltic sedimentary rocks on the surface of Mars. The selected lines are sensitive to salt concentration, providing a method for tracking relative changes in salt content above detection limits of about 5–10 wt % salt for chlorides (3–6 wt % Cl), ~20 wt % salt for carbonates (2 wt % C), and 5–30 wt % salt for sulfates (1–8 wt % S). Absolute univariate quantification of the salt content of samples of unknown composition may be inaccurate for high salt concentrations due to differing trends in the calibration curves for different cation elements in salt + basalt mixtures. The basaltic matrix appeared to be less important in determining the calibration curves, following normalization by the total emission. The amount of increase in continuum emission over successive laser shots into the target may also track with salt content in the sample, providing an empirical method to identify potential samples with high salt, but requires further characterization to be developed into a useful method of analysis. These results suggest that as a survey tool, ChemCam should be able to track significant changes in the salt content of the bulk rock in the sedimentary units of Gale crater by observation of selected emission lines of Cl, C, and S in the LIBS spectra. Distinguishing between salts based on identification of specific Cl, C, and S lines would provide important implications regarding ancient environmental conditions of the region. These laboratory results will thus feed forward to in situ rover investigations and analyses of LIBS data returned from Mars.

Acknowledgments

Thanks to Mike Baker for supplying the K1919 end-member and George Rossman for end-member acquisition advice. Thanks to the entire MSL ChemCam team for feedback throughout this project. Thanks to the anonymous reviewers for their valuable suggestions that have improved this document. This work was supported by a NASA MSL Participating Scientist Program grant to B.L. Ehlmann, a National Science Foundation Graduate Research Fellowship under grant DGE-11444469 to D.E. Anderson, and by contract from NASA's Mars Exploration Program to R.C. Wiens and S.M. Clegg. Supporting data are included as supporting information; any additional information may be obtained from D.E. Anderson (e-mail: deanders@caltech.edu).

References

Anderson, R. B., and J. F. Bell III (2010), Geologic mapping and characterization of Gale crater and implications for its potential as a Mars Science Laboratory landing site, *Mars*, *5*, 76–128, doi:10.1555/mars.2010.0004.

Beck, P., et al. (2016), Carbon detection with ChemCam: Laboratory studies and Mars results, paper presented at 47th Lunar and Planetary Science Conference, The Woodlands, Tex.

Carranza, J. E., and D. W. Hahn (2002), Sampling statistics and considerations for single-shot analysis using laser-induced breakdown spectroscopy, *Spectrochim. Acta Part B*, *57*, 779, doi:10.1016/S0584-8547(02)00007-1.

Clegg, S. M., et al. (2013), High calcium phase observations at Rocknest with ChemCam, paper presented at 44th Lunar & Planetary Science Conference, The Woodlands, Tex.

Clegg, S. M., et al. (2017), Recalibration of the Mars Science Laboratory ChemCam instrument with an expanded geochemical database, *Spectrochim. Acta Part B*, *129*, 64–85, doi:10.1016/j.sab.2016.12.003.

Corsi, M., G. Cristoforetti, M. Hidalgo, D. Iriarte, S. Legnaioli, V. Palleschi, A. Salvetti, and E. Tognoni (2005), Effect of laser-induced crater depth in laser-induced breakdown spectroscopy emission features, *Appl. Spectrosc.*, *59*, 853–860, doi:10.1366/0003702054411607.

Cousin, A., O. Forni, S. Maurice, O. Gasnault, C. Fabre, V. Sautter, R. C. Wiens, and J. Mazoyer (2011), Laser induced breakdown spectroscopy library for the Martian environment, *Spectrochim. Acta Part B*, *66*, 805–814, doi:10.1016/j.sab.2011.10.004.

Cremers, D. A., and L. J. Radziemski (2013), *Handbook of Laser-Induced Breakdown Spectroscopy*, 2nd ed., John Wiley, Oxford, U. K., doi:10.1002/9781118567371.

Dyar, M. D., J. M. Tucker, S. Humphries, S. M. Clegg, R. C. Wiens, and M. D. Lane (2011), Strategies for Mars remote Laser-Induced Breakdown Spectroscopy analysis of sulfur in geological samples, *Spectrochim. Acta Part B*, *66*, 39–56, doi:10.1016/j.sab.2010.11.016.

Ehlmann, B. L., and C. S. Edwards (2014), Mineralogy of the Martian surface, *Annu. Rev. Earth Planet. Sci.*, *42*, 291–315, doi:10.1146/annurev-earth-060313-055024.

Fabre, C., et al. (2014), In situ calibration using univariate analyses based on the onboard ChemCam targets: First prediction of Martian rock and soil compositions, *Spectrochim. Acta Part B*, *99*, 34–51, doi:10.1016/j.sab.2014.03.014.
Forni, O., et al. (2015), First detection of fluorine on Mars: Implications for Gale Crater's geochemistry, *Geophys. Res. Lett.*, *42*, 1020–1028, doi:10.1002/2014GL062742.
Frydenvang, J., et al. (2016), Discovery of silica-rich lacustrine and eolian sedimentary rocks in Gale Crater, Mars, paper presented at 47th Lunar and Planetary Science Conference, The Woodlands, Tex.
Gaft, M., L. Nagli, N. Eliezer, Y. Groisman, and O. Forni (2014), Elemental analysis of halogens using molecular emission by laser-induced breakdown spectroscopy in air, *Spectrochim. Acta Part B*, *98*, 39–47, doi:10.1016/j.sab.2014.05.011.
Gasda, P. J., et al. (2016), Potential link between high-silica diagenetic features in both eolian and lacustrine rock units measured in Gale Crater with MSL, paper presented at 47th Lunar and Planetary Science Conference, The Woodlands, Tex.
Gendrin, A., et al. (2005), Sulfates in Martian layered terrains: The OMEGA/Mars Express View, *Science*, *307*, 1587–1591, doi:10.1126/science.1109087.
Gill, P. E., W. Murray, and M. H. Wright (1981), *Practical Optimization*, pp. 36–137, Academic Press, London.
Hecht, M. H., et al. (2009), Detection of perchlorate and the soluble chemistry of Martian soil at the Phoenix lander site, *Science*, *325*, 64–67, doi:10.1126/science.1172466.
Kramida, A., Y. Ralchenko, J. Reader, and NIST ASD Team (2015), *NIST Atomic Spectra Database (version 5.3)*, [2016]. National Institute of Standards and Technology, Gaithersburg, Md. [Available at http://physics.nist.gov/asd, Accessed 2016.]
Lanza, N. L., R. C. Wiens, S. M. Clegg, A. M. Ollila, S. D. Humphries, H. E. Newsom, and J. E. Barefield (2010), Calibrating the ChemCam laser-induced breakdown spectroscopy instrument for carbonate minerals on Mars, *Appl. Optics*, *49*, C211, doi:10.1364/AO.49.00C211.
Lanza, N. L., et al. (2015), Understanding the signature of rock coatings in laser-induced breakdown spectroscopy data, *Icarus*, *249*, 62–73, doi:10.1016/j.icarus.2014.05.038.
Lasue, J., R. C. Wiens, S. M. Clegg, D. T. Vaniman, K. H. Joy, S. Humphries, A. Mezzacappa, N. Melikechi, R. E. McInroy, and S. Bender (2012), Remote laser-induced breakdown spectroscopy (LIBS) for lunar exploration, *J. Geophys. Res.*, *117*, E01002, doi:10.1029/2011JE003898.
Le Deit, L., E. Hauber, F. Fueten, M. Pondrelli, A. P. Rossi, and R. Jaumann (2013), Sequence of infilling events in Gale Crater, Mars: Results from morphology, stratigraphy, and mineralogy, *J. Geophys. Res. Planets*, *118*, 2439–2473, doi:10.1002/2012JE004322.
Leshin, L. A., et al. (2013), Volatile, isotope, and organic analysis of Martian fines with the Mars Curiosity Rover, *Science*, *341*, 1–9, doi:10.1126/science.1238937.
Massart, D. L., B. G. M. Vandeginste, L. M. C. Buydens, S. De Jong, P. J. Lewi, and J. Smeyers-Verbeke (Eds) (1998), *Handbook of Chemometrics and Qualimetrics: Part A*, Elsevier, New York.
Maurice, S., et al. (2012), The ChemCam Instrument Suite on the Mars Science Laboratory (MSL) Rover: Science objectives and mast unit description, *Space Sci. Rev.*, *170*, 95–166, doi:10.1007/s11214-012-9912-2.
McWorter, D. B., and D. K. Sunada (1977), *Ground-Water Hydrology and Hydraulics*, Water Resources Publications, Highlands Ranch, Colo.
Meslin, P.-Y., et al. (2016), Calibration of the fluorine, chlorine, and hydrogen content of apatites with the ChemCam LIBS instrument, paper presented at 47th Lunar and Planetary Science Conference, The Woodlands, Tex.
Milliken, R. E., J. P. Grotzinger, and B. J. Thomson (2010), Paleoclimate of Mars as captured by the stratigraphic record in Gale Crater, *Geophys. Res. Lett.*, *37*, L04201, doi:10.1029/2009GL041870.
Ming, D. W., et al. (2014), Volatile and organic compositions of sedimentary rocks in Yellowknife Bay, Gale Crater, Mars, *Science*, *343*, 1245267, doi:10.1126/science.1245267.
Nachon, M., et al. (2014), Calcium sulfate veins characterized by ChemCam/Curiosity at Gale crater, Mars, *J. Geophys. Res. Planets*, *119*, 1991–2016, doi:10.1002/2013JE004588.
Nachon, M., et al. (2017), Chemistry of diagenetic features analyzed by ChemCam at Pahrump Hills, Gale craters, Mars, *Icarus*, *281*, 121–136, doi:10.1016/j.icarus.2016.08.026.
Newsom, H. E., et al. (2016), The materials at an unconformity between the Murray and Stimson Formations at Marias Pass, Gale Crater, Mars, paper presented at 47th Lunar and Planetary Science Conference, The Woodlands, Tex.
Newville, M., T. Stensitzki, D. B. Allen, and A. Ingargiola (2014), *LMFIT: Non-linear least-square minimization and curve-fitting for Python*, Zenodo, doi:10.5281/zenodo.11813, Accessed 2016.
Ollila, A. M., J. G. Blank, R. C. Wiens, J. Lasue, H. E. Newsom, S. M. Clegg, A. Cousin, and S. Maurice (2011), Preliminary results on the capabilities of the ChemCam laser-induced breakdown spectroscopy (LIBS) instrument to detect carbon on Mars, paper presented at the 42nd Lunar and Planetary Science Conference, The Woodlands, Tex.
Ollila, A. M., et al. (2013), Early results from Gale Crater on ChemCam detections of carbon, lithium, and rubidium, paper presented at 44th Lunar and Planetary Science Conference, The Woodlands, Tex.
Rapin, W., et al. (2016), Hydration of calcium sulfates in Gale Crater: Identification of bassanite veins, *Earth Planet. Sci. Lett.*, *452*, 197–205, doi:10.1016/j.epsl.2016.07.045.
Schröder, S., S. G. Pavlov, I. Rauschenbach, E. K. Jessberger, and H.-W. Hübers (2013), Detection and identification of salts and frozen salt solutions combining laser-induced breakdown spectroscopy and multivariate analysis methods: A study for future Martian exploration, *Icarus*, *223*, 61–73, doi:10.1016/j.icarus.2012.11.011.
Schröder, S., et al. (2015), Hydrogen detection with ChemCam at Gale crater, *Icarus*, *249*, 43–61, doi:10.1016/j.icarus.2014.08.029.
Schröder, S., K. Rammelkamp, A. Cousin, D. Vogt, P.-Y. Meslin, S. Maurice, and H.-W. Hübers (2017), LIBS analysis of perchlorates and chlorides in soil in Mars-like conditions, paper presented at the 48th Lunar and Planetary Science Conference, The Woodlands, Tex.
Singh, J. P., and S. N. Thakur (2007), *Laser-Induced Breakdown Spectroscopy*, Elsevier Science, Oxford, U. K.
Sobron, P., A. Wang, and F. Sobron (2012), Extraction of compositional and hydration information of sulfates from laser-induced plasma spectra recorded under Mars atmospheric conditions—Implications for ChemCam investigations on Curiosity rover, *Spectrochim. Acta Part B*, *68*, 1–16, doi:10.1016/j.sab.2012.01.002.
Stern, J. C., et al. (2015), Evidence for indigenous nitrogen in sedimentary and aeolian deposits from the Curiosity rover investigations at Gale crater, Mars, *Proc. Natl. Acad. Sci. U.S.A.*, *112*, 4245–4250, doi:10.1073/pnas.1420932112.
Thomas, N. H., B. L. Ehlmann, and D. E. Anderson (2015), Characterization of hydrogen abundance in LIBS data, paper presented at 46th Lunar & Planetary Science Conference, The Woodlands, Tex.
Thomas, N. H., et al. (2016), Characterization of hydrogen in basaltic materials with laser-induced breakdown spectroscopy (LIBS), paper presented at 47th Lunar and Planetary Science Conference, The Woodlands, Tex.
Thomson, B. J., N. T. Bridges, R. Milliken, A. Baldridge, S. J. Hook, J. K. Crowley, G. M. Marion, C. R. de Souza Filho, A. J. Brown, and C. M. Weitz (2011), Constraints on the origin and evolution of the layered mound in Gale Crater, Mars using Mars Reconnaissance Orbiter data, *Icarus*, *214*, 413–432, doi:10.1016/j.icarus.2011.05.002.

Tucker, J. M., M. D. Dyar, M. W. Schaefer, S. M. Clegg, and R. C. Wiens (2010), Optimization of the laser-induced breakdown spectroscopy for rapid geochemical analysis, *Chem. Geol.*, *277*, 137–148, doi:10.1016/j.chemgeo.2010.07.016.

Vaniman, D. T., et al. (2014), Mineralogy of a Mudstone at Yellowknife Bay, Gale Crater, Mars, *Science*, *343*, 1243480, doi:10.1126/science.1243480.

Vogt, D., K. Rammelkamp, S. Schröder, and H.-W. Hübers (2017), Suitability of molecular emission in laser-induced breakdown spectroscopy for the quantification of chlorine under Martian conditions, paper presented at 48th Lunar & Planetary Science Conference, The Woodlands, Tex.

Wiens, R. C., et al. (2012), The ChemCam instrument suite on the Mars Science Laboratory (MSL) rover: Body unit and combined system tests, *Space Sci. Rev.*, *170*, 167–227, doi:10.1007/s11214-012-9902-4.

Wiens, R. C., et al. (2013), Pre-flight calibration and initial data processing for the ChemCam laser-induced breakdown spectroscopy instrument on the Mars Science Laboratory rover, *Spectrochim. Acta Part B*, *82*, 1–27, doi:10.1016/j.sab.2013.02.003.

Yen, A. S., et al. (2005), An integrated view of the chemistry and mineralogy of Martian soils, *Nature*, *436*, 49–54, doi:10.1038/nature03637.